EÖTVÖS LORÁND UNIVERSITY

FACULTY OF INFORMATICS

DEPARTMENT OF CARTOGRAPHY AND GEOINFORMATICS

A Google Earth Engine-Based Interactive Web Application for Continuously Monitoring the GERD Reservoir in Ethiopia

Submitted by

Muhammed Abdelaal

Student of Cartography MSc

Supervised by

Prof. András Jung

ELTE Department of Cartography and Geoinformatics

Budapest, 2022

To my parents, three sisters, and beloved fiancée.

Abstract

This work presents an automated processing chain surface water mapping of the GERD reservoir in Ethiopia using Sentinel-1 SAR. A user-friendly interactive web application is built upon this algorithm to allow the public to continuously monitor the waterbody volume variation in this study area. The application leverages the powerful computational capabilities of Google Earth Engine and its continually updated datasets.

Contents

List of Figures

List of Tables

1. Introduction

1.1 Background

Egypt is in a water crisis that threatens its exponentially growing population's lives and future. The current population is around 105 million people. It is expected to double by 2061, given that the rate of population change is 1.8% per year, which annually increases the population by about two million people(United Nations Population Fund, 2022). Consequently, the demand for freshwater alarmingly rises, leading to a disturbing decline in the per capita water supply, increasing Egypt's food security risk since the agriculture sector consumes about 79% of Egypt's freshwater share(The World Bank, 2017).

The Nile River is the primary resource of Egypt's freshwater that contributes about 97% of its renewable water resources. As Figure 1 illustrates, it originates outside Egypt's borders, starting from the center of Africa and traveling through eleven countries: Tanzania, Uganda, Rwanda, Burundi, the Democratic Republic of the Congo, Kenya, Ethiopia, Eritrea, South Sudan, Sudan, and Egypt. It has two main tributaries — the White Nile, which starts from Uganda Victoria Lake, and the Blue Nile, which begins at Ethiopia Lake Tana. These two tributaries unify at Khartoum, the capital of Sudan, and the river continues flowing from south to north through Sudan and Egypt till it empties into the Mediterranean Sea. The Ethiopian highlands provide 86% of the Nile flow, while the contribution from the Equatorial Lakes region is only 14%(Swain, 2011).

1.2 Problem Statement

Along with the negative impacts of climate change and the rapid population growth on the Egyptian renewable water resources, in 2011, another challenge had emerged when the Ethiopian government announced the beginning of construction of a large-scale hydroelectric dam, the Grand Ethiopian Renaissance Dam (GERD), on the Blue Nile with a reservoir of a total capacity of 74 billion m^3 (Elsayed et al., 2020). The heart of the dispute is the GERD reservoir filling period, which is five years, with 35 billion m^3 of water being released to downstream countries each year while the dam is being filled, as announced by the Ethiopian government. On the other hand, Egypt

demands that the filling process is over seven years to retain the same amount of annual water supply that does not negatively affect irrigation and hydropower generation(Roussi, 2019).

Figure 1. Map of the Nile River basin countries and its primary water resources: Uganda Victoria Lake and Ethiopia Tana Lake.

Due to the lack of cooperation and coordination and unilateral decision-making, the first two phases of the reservoir filling were completed without reaching a binding agreement over the GERD reservoir filling among Egypt, Sudan, and Ethiopia, in July 2020 and July 2021, respectively. Accordingly, this non-cooperative behavior led to inconsistent and unreliable information regarding the start and end of each filling phase and the amount of water stored. After

the second filling, Ethiopia claimed that it achieved its target for 2021 by storing 13.5 billion m^3, and it is expected to reach total capacity by 2023. However, some Egyptian experts doubt the claims(Al Jazeera, 2022).

1.3 Satellite Remote Sensing

Satellite remote sensing plays an integral role in water resources management as a reliable information source about surface water dynamics for decision-makers and the public. It can timely and continuously monitor surface water and its change across large areas. In recent years, with launching new remote sensing satellites, its role has become more promising since more data become freely and openly available, enabling the implementation of more accurate surface water mapping and satellite-derived time series analysis of water volume variations.

The surface water extent maps can be derived from two main remotely sensed data sources: the optical and the Synthetic Aperture Radar (SAR) Earth Observation (EO) sensors. The former are passive sensors that rely on the natural energy coming from the sun and mainly detect energy from the visible, near-infrared(NIR), and shortwave-infrared(SWIR) portions of the electromagnetic spectrum. The typical optical data sources include Landsat-5/7/8 and Sentinel-2. On the other hand, SAR (e.g., Sentinel-1) is an active remote sensing technique that provides its energy source for illumination. It emits microwave electromagnetic energy to form complex images of terrain reflectivity(Jiang et al., 2021). This complexity of the SAR images may vary depending on many factors: incidence angle, terrain structure, and surface roughness, which makes the image relatively challenging to interpret compared to the optical images that are preferred in good weather conditions due to their straightforward interpretability. However, SAR sensors can provide day-and-night and cloud-free images, which are more suitable and effective in systematic monitoring applications requiring dense time series analysis, especially in regions with persistent cloud cover (e.g., Ethiopia).

1.4 Google Earth Engine

In the last decade, the processing of a massive amount of satellite imagery has become more manageable and accessible for many scientists and independent researchers due to the free availability of petabytes-scale archives of remote sensing data and the establishment of Google Earth Engine (GEE) towards the end of 2010.

GEE is a cloud-computing platform powered by Google Cloud Platform (GCP), established to store and process planetary-scale geospatial datasets, enabling researchers to process vast amounts of satellite imagery. Unlike other remote sensing software, GEE enables researchers to quickly disseminate their results to other researchers, policymakers, and even the public through dynamic, publicly accessible, and user-friendly interface applications (Gorelick et al., 2017). GEE public data archive includes over 40 years of historical satellite imagery and widely used geospatial datasets, including complete archives of data from Landsat5/7/8, Sentinel-1, and Sentinel-2, as well as other environmental, geophysical, and demographic datasets. To access and analyze the data from the public catalog, users can connect to the GEE service through a web-based interactive development environment(IDE) via an application programming interface(API) available in Python and JavaScript. These client libraries for Python and JavaScript translate the analysis to Earth Engine requests. Then, the computation runs in an extensive parallel processing system that subdivides and distributes it to many processors, enabling high computational capabilities.

1.5 Objective and the Research Product

This work aims to take the most advantage of GEE computational capabilities and its freely available and continuously updated satellite imagery to serve as a reliable information source about the GERD reservoir surface water dynamics, providing continuous monitoring of the GERD reservoir surface water extent and its water volume variations. The final product of this work comes in two forms: an application programming interface software and an interactive web-based user-friendly application. The former is an open-source Python package that contains a collection of software functions built upon GEE Python API to access the satellite imagery from the GEE

public data catalog and send the analysis requests. Then, the user-friendly application is built upon this Python package.

The final product was named after the ancient Egyptian name of the Nile River: Iteru. The source code of the Python package (Iteru) and the application (IteruApp), and the user-friendly application (Figure 2) can be accessed from the following links, respectively:

- Iteru : (https://github.com/MuhammedM294/Iteru)
- IteruApp : (https://github.com/MuhammedM294/IteruApp)
- Streamlit-IteruApp: (https://share.streamlit.io/muhammedm294/iteruapp)

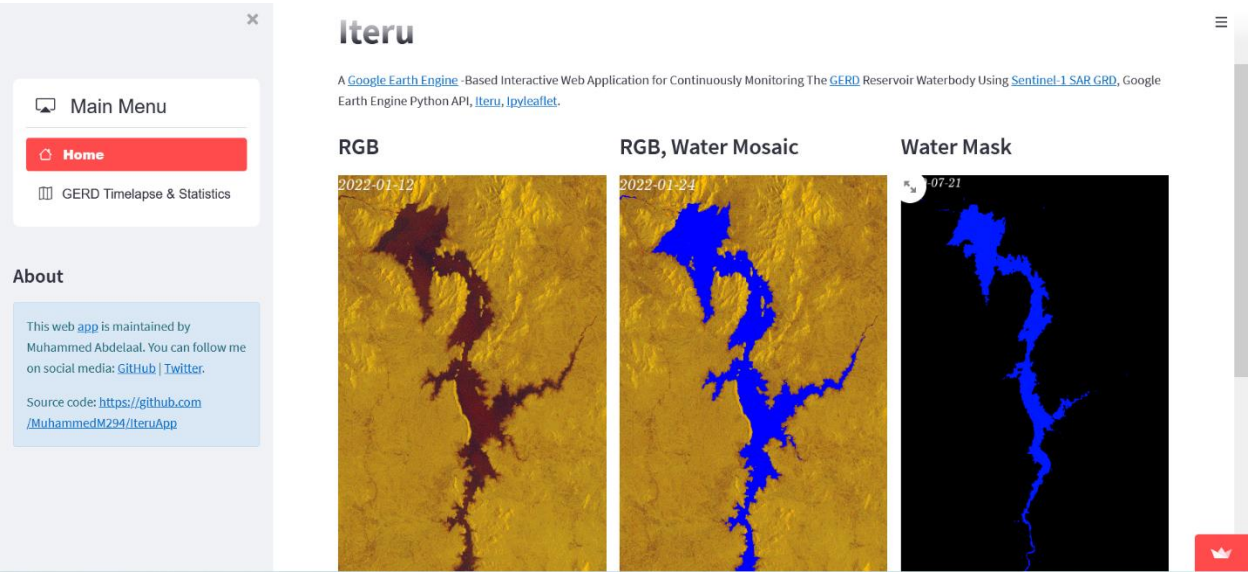

Figure 2. The home page of Streamlit-Iteruapp

The development environment and the ancillary software used in this work:

- Jupyter Notebook: An open-source web-based interactive development environment.
- Visual Studio Code: A standalone source-code editor
- Ipyleaft/geemap: An open-source Python package for interactive web mapping
- Streamlit: An open-source application framework for data scientists to deploy and share their application

1.6 Thesis structure

The rest of the thesis is organized into seven other chapters. Chapter two introduces the study area and the primary datasets utilized in this work. In chapter three, an overview of the principles of radar imaging and the synthetic aperture radar is presented. Also, a brief description of the Sentinel-1 missions and its acquisition modes and processing levels is contained. Chapter four demonstrates the preprocessing steps performed on the Sentinel-1 SAR imagery before detecting surface water extent. The fifth chapter elaborates on the principles of waterbody detection from Sentinel-1 SAR imagery and the used algorithm for that purpose. Chapter six comprehensively explains the workflow of IteruApp for automatically mapping surface water extent from Sentinel-1 SAR imagery and computing the waterbody volume. In chapter seven, the performance of the VV and VH polarization bands in inland waterbody detection is evaluated using Sentinel-2 imagery as a validation dataset. Finally, chapter eight presents the conclusions and suggests further research directions.

2. Study area and Datasets

2.1 Study Area

The Grand Ethiopian Renaissance Dam (GERD) is located on the Blue Nile within the Benishangul-Gumuz Region of Ethiopia, approximately 10 km southeast of the Sudan-Ethiopia border (Figure 3). This region is characterized by a tropical savanna climate, in which the rainy seasons extend from May to October.

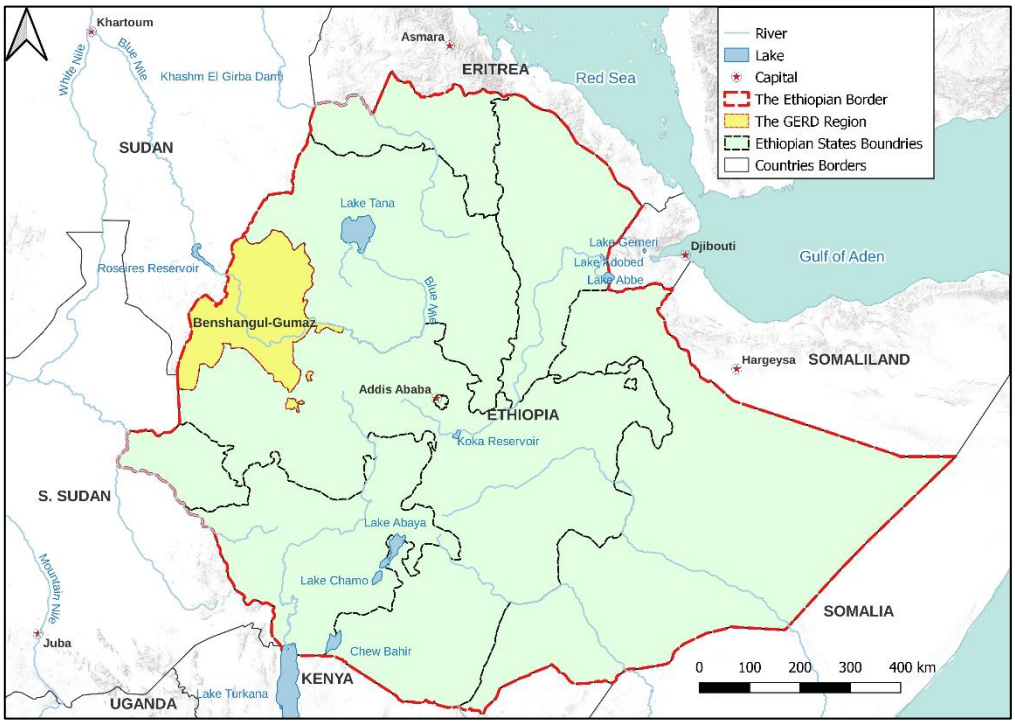

Figure 3. Map of Ethiopia showing the Benishangul-Gumuz Region

The GERD area extends from 35º 00` 29.68" to 35º 23` 13.53" E and 10º 31` 19.91" to 11º 15` 59.72" N. Figure 4 demonstrates that the project consists of two dams: the main dam and a saddle dam. The main dam is a gravity dam constructed from roller-compacted concrete that extends around 1800 m long at the crest elevation with a maximum height of 175m. The saddle dam is a concrete-faced rockfill dam with a height of 60m and around 5 km long, constructed to permit a higher water elevation and storage.

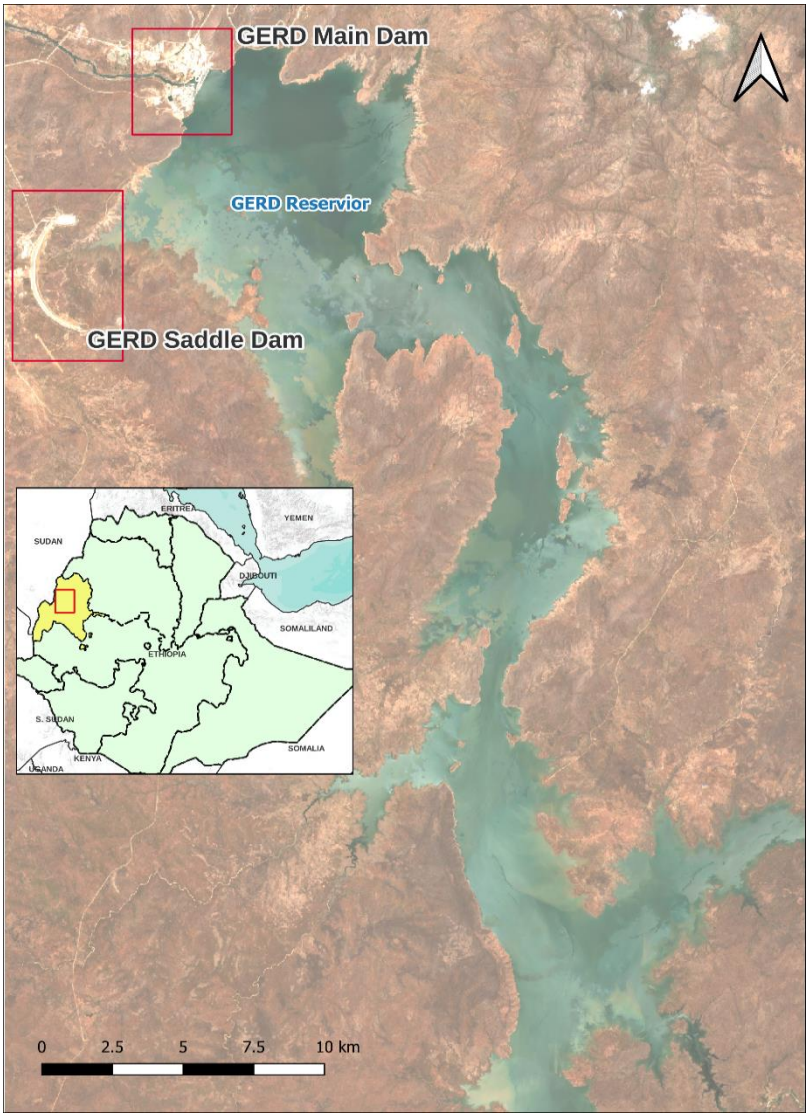

Figure 4. Sentinel-2 image shows the GERD area. (Acquired on 14-Apr-2022)

2.2 Datasets

There are mainly two datasets ingested in GEE utilized in this work(Table 1):

1. Sentinel-1 SAR Ground Range Detected (GRD) images.
2. FABDEM(Hawker et al., 2022): a new digital surface model with artifacts from forests and buildings removed.

Table 1. The main GEE datasets utilized in the work

Dataset	Provider	Purpose
Sentinel-1 SAR GRD	The European Space Agency	- For surface water extent mapping.
FABDEM	The University of Bristol, England.	- To determine the surface water level. - To calculate water body volume.

3. Synthetic Aperture Radar (SAR)

3.1 Imaging Radar Overview

The microwave portion of the electromagnetic spectrum extends from a wavelength of approximately 1 cm to 1 m. Compared to the visible and infrared, this relatively long wavelength provides the capability to penetrate through the clouds without being affected by the atmospheric scattering. Therefore, under most weather conditions, microwave energy can be detected, allowing monitoring of the Earth's surface at any time. Accordingly, active microwave sensors have two primary advantages over optical sensors: they can operate under most weather conditions and provide day-and-night images since they have their energy source to illuminate their targets at the Earth's surface.

Radar, which stands for radio detection and ranging, is the most common form of imaging active microwave sensors. It can form images of the Earth's surface by transmitting microwave signals toward the targets, then receiving their reflection (backscatter portion of the signals). The time delay between the transmission and reception determines the distances (ranges) to the targets, and the backscatter intensity distinguishes the different targets. That is to say, a radar device essentially consists of a transmitter, an antenna, a receiver, and a recorder. The transmitter produces successive short pulses of microwave signals at a given frequency. After that, the antenna focuses the signals into a narrow beam of microwave energy, transmits it to illuminate the surface, and receives its echo from the terrain. Then, the receiver accepts the backscattered energy, then filters and amplifies it as required. Finally, the recorder records and processes the backscattered signals, displaying them as images.

Additionally, the radar can compare the transmitted signals of a known wavelength with the received ones, detecting their frequency and polarization change. The polarization refers to the orientation of the electric field (E) (Figure 5), which may be horizontal or vertical. Most radars can transmit the microwave signals and receive the backscattered signals either vertically (V) or horizontally (H), constituting four combinations of polarization: HH, VV, HV, and VH. The first

letter indicates the transmission polarization in each combination, and the second letter indicates the reception polarization(Radar Polarimetry, 2015).

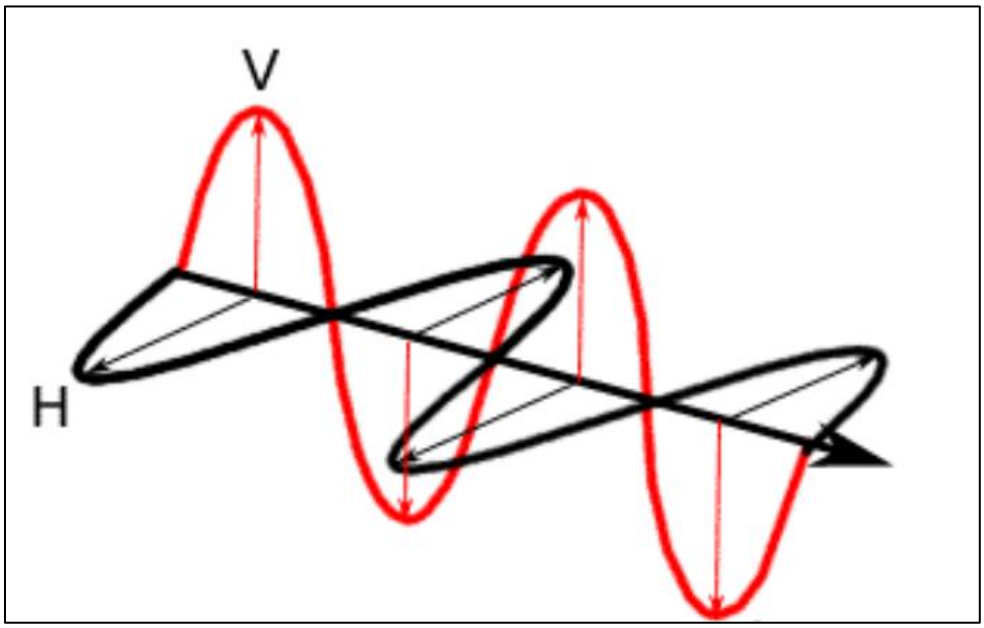

Figure 5. The orientation of the electric field (polarization).

Figure 6 illustrates the side-looking imaging technique of the imaging radar. While traveling forward in the flight direction, the radar antenna is pointed away from the nadir by a so-called look angle θ_L, unlike most of the scanning systems of the optical remote sensing, which direct their sensors toward the nadir. The darker grey area in Figure 6 corresponds to an immediate area illuminated by the microwave beam, also referred to as the antenna footprint. Its resolution in the cross-track direction (range resolution) is defined by the length of the generated pulses (system wavelength) in the slant range direction. The along-track resolution (azimuth resolution) is defined by the microwave beamwidth, which is inversely proportional to the side length of the antenna, which is also referred to as the aperture. Therefore, a longer antenna will generate a narrower beamwidth, resulting in a finer resolution in the azimuth direction. A shorter pulse length will achieve a finer resolution in the range direction. Nevertheless, the length of the antenna that can be carried on airborne and space-borne is restricted to one to two and 10-15 meters, respectively. Based on this length, the achieved azimuth resolution is impractical for most Earth observation applications; for example, a 60 m resolution needs an excessive antenna length of about 600 m(The SAR Handbook, 2018). This problem was overcome by the synthetic aperture principle,

which, essentially, employs the forward motion of the radar platform along its track and its sequence of acquisitions to synthesize a much longer antenna (the so-called synthetic aperture).

This principle enables modern radars, typically synthetic aperture radar (SAR), to achieve higher ground resolutions, considering their specific design.

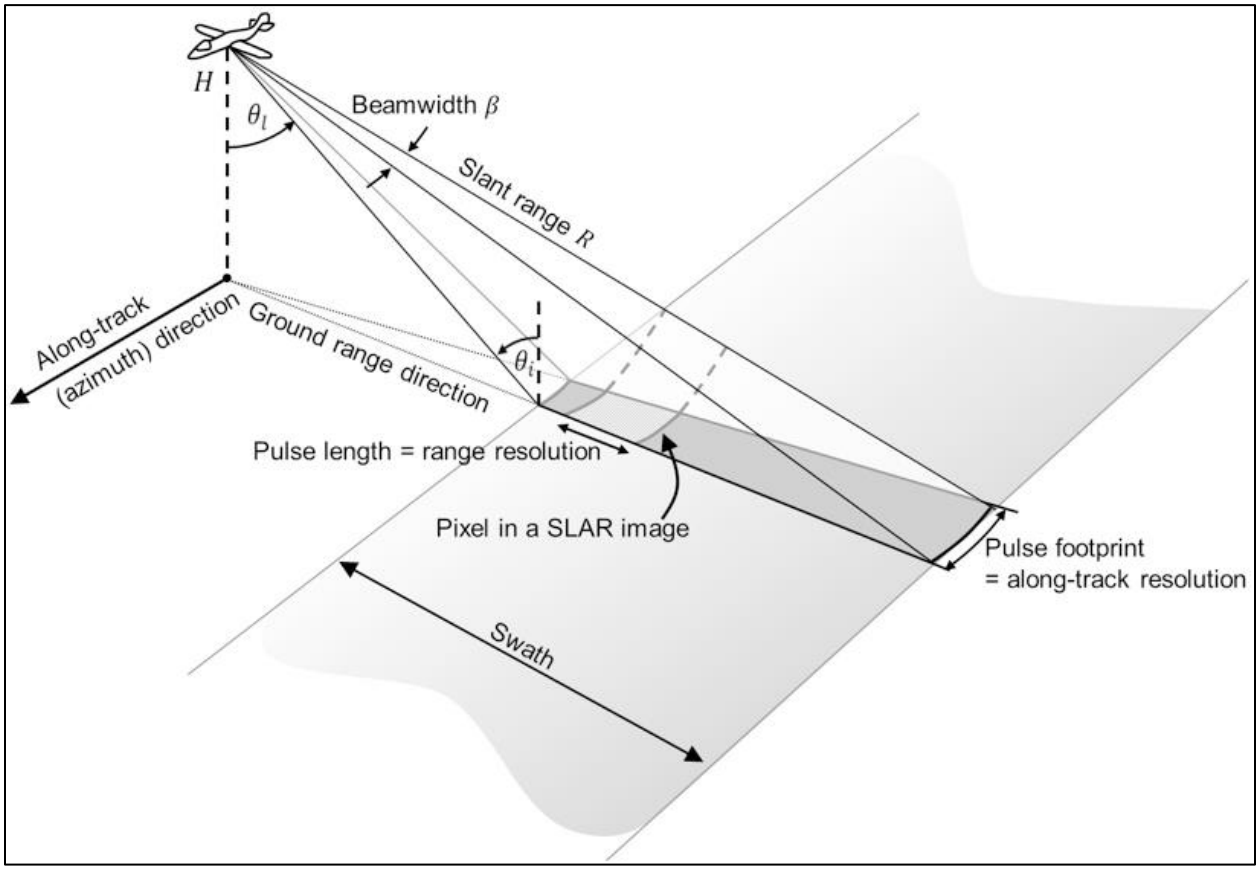

Figure 6. The side-looking viewing geometry of the imaging radar systems (THE SAR HANDBOOK Comprehensive Methodologies for Forest Monitoring and Biomass Estimation, 2018).

In radar imagery, each image consists of pixels of different brightness values that depend on the reflected portion of the transmitted energy. The strength of reflected energy may vary depending on several factors related to the surface properties, such as terrain structure and surface roughness, and other parameters related to the radar system itself, such as frequency, polarization, and the viewing geometry (the incidence angle). In summary, radar sensors can generate energy at different wavelengths ranging from 1 cm to 1 m and transmit and receive it in four polarization combinations. Both factors—the wavelength and polarization—fundamentally control how radar can sense the targets on the Earth's surface, providing different and integral data about them.

Applying the synthetic aperture principle enables the radar systems to obtain more efficient and practical observations from Earth-orbiting satellites by overcoming the azimuth resolution problem; nevertheless, these systems are more complex and expensive to manufacture and operate.

3.2 Sentinel-1 SAR

3.2.1 Overview

Sentinel-1 is one of the fleets of Sentinel satellite missions jointly initiated by the European Commission (EC) and the European Space Agency (ESA). This project is funded by the European Union (EU) and the ESA Member States, and various ESA establishments participated in developing, operating, and managing this mission. It is a constellation of two satellites sharing the same orbital plane with a 180° orbital phasing difference at around 700 km altitude. Each satellite is in a near-polar, sun-synchronous orbit, with a 12-day repeat cycle and 175 orbits per cycle. The two satellites—Sentinel-1A and Sentinel-1B—were launched on 3 April 2014 and 25 April 2016, respectively. Due to a technical malfunction, Sentinel-1B is currently unavailable since it took out of service in December 2021, so a third Sentinel-1 satellite (Sentinel-1C) will be launched in the first half of 2023. Each carries an advanced radar instrument, a C-band Synthetic Aperture Radar (SAR) operating at a frequency of 5.405 GHz, to provide high-resolution SAR images of all global landmass, coastal zones, and ships routes. The Sentinel-1 mission's main objective is to provide information to various services for applications in the monitoring of climate change, land, and maritime and emergency management.

3.2.2 Acquisition Modes

Sentinel-1 functions in four acquisitions modes (Figure 7)(User Guides - Sentinel-1 SAR - Acquisition Modes, 2022):

- Interferometric Wide Swath (IW) mode is the prime acquisition mode used in land-related applications. It captures data in single-polarization (HH or VV) and dual-polarization (HH+HV or VV+VH) with a swath of 250 km at a spatial resolution of 5 m by 20 m.

- Wave Mode (WV) is the primary operational mode used in ocean-related applications. It acquires the observations in 20 km by 20 km scenes at a spatial resolution of 5 m by 5 m in single polarization (HH or VV).

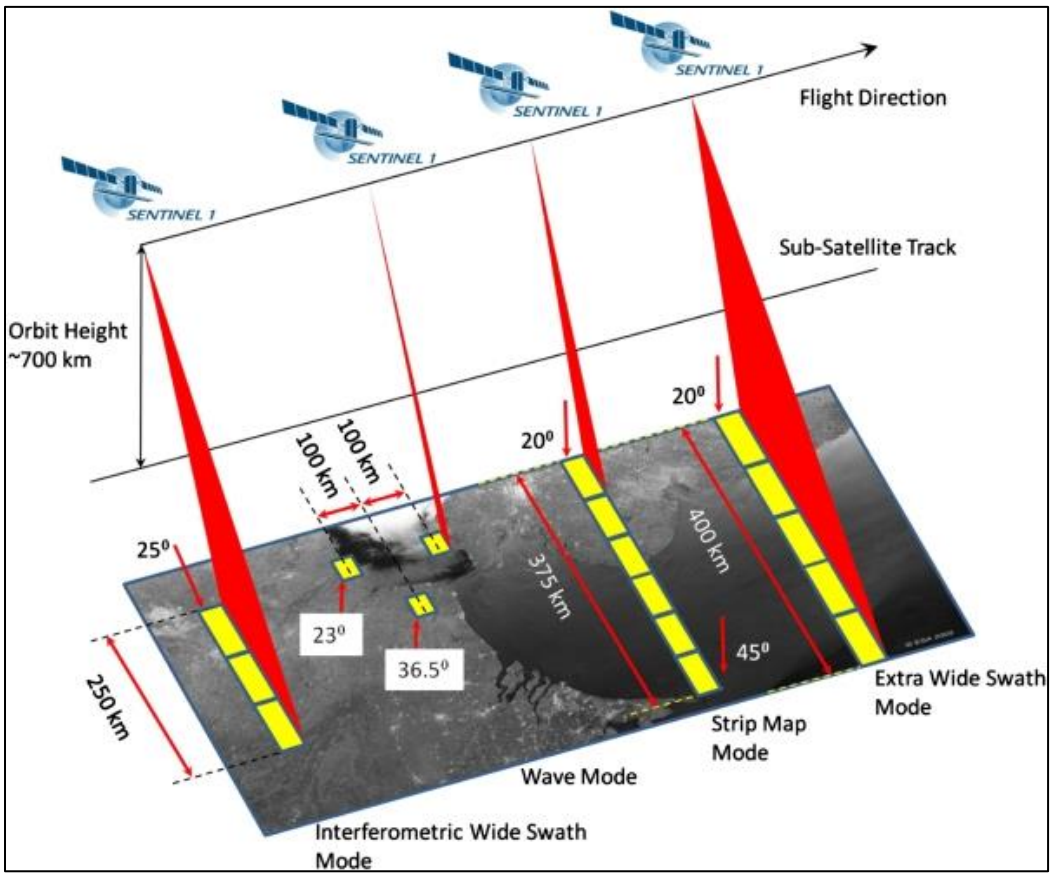

Figure 7. Sentinel Products Acquisition Modes – (User Guides - Sentinel-1 SAR - Acquisition Modes - Sentinel Online - Sentinel Online, 2022).

- Stripmap (SM) mode is used in exceptional cases only to capture data over islands to manage emergency actions. It captures the data in single and dual polarization with a swath width of 80 km at a spatial resolution of 5 m by 5 m.

- Extra Wide Swath (EW) mode has the same imaging technique as the IW mode, but it collects observations over a wider area using five sub-swaths compared to three sub-swaths of the IW mode. It captures the data in single and dual polarization with a 400 km swath at a 20 m by 40 m spatial resolution.

3.2.3 Processing Levels

There are three primary processing levels of the data acquired in the IW, SM, and EW modes(User Guides - Sentinel-1 SAR, 2022):

- Level-0 is considered the basis for the other higher processing levels. Its products consist of unfocused and compressed raw data that includes information about orbit, altitude, noise, internal calibration, and echo source packets.
- Level-1 is produced by transforming the raw data from level-0 using various algorithms and the Sentinel-1 Instrument Processing Facility(IPF). Its focused data can be processed into either Single Look Complex (SLC) or Ground Range Detected (GRD).
    1. SLC is provided in slant range geometry, which is the natural radar range observation coordinate(line of sight from radar to the reflected object on the Earth's surface). The spatial resolution of its products depends upon the acquisition mode and varies in range and azimuth direction. For instance, the spatial resolution in the IW mode ranges from 2.7 × 22 m to 3.5 ×22 m in range and azimuth direction, respectively, and resampled to a pixel spacing grid of 2.3 ×14.1 m.
    2. GRD is composed of focused SAR data that has been observed, multi-looked to reduce noise(speckle), and projected to ground range using World Geodetic Datum 1984 (WGS84). Its products have three different resolutions based on the acquisition mode: full, high, and medium resolution. For example, the high resolution of the IW mode is 20×22 m and resample to a pixel spacing grid of 10 ×10 m.

    The GEE data catalog only contains GRD data, which is the main dataset for the whole work.
- Level-2 is generated from level-1 and comprises geolocated geophysical products, which provide information about ocean wind, waves, and currents.

4. Sentinel-1 SAR Preprocessing

4.1 GEE Sentinel-1 SAR Preprocessing

GEE plays a vital role in widening the user community of Sentinel-1 imagery by providing Analysis-Ready-Data(ARD). The intensive burden of preprocessing raw data is removed, letting the user focus on the actual information extraction(Vollrath et al., 2020). GEE data catalog provides a preprocessed Sentinel-1 C-band image collection from 3 October 2014 thus far. This image collection consists of Level-1 Ground Range Detected (GRD) scenes. The scenes are captured using three acquisition modes with a revisiting time of 6-12 days, and the spatial resolution may be one of 3 resolutions (10, 25, or 40 m). Each scene includes an incidence angle band, and it may contain one or two out of 4 polarization bands(Sentinel-1 SAR GRD | Earth Engine Data Catalog):

1. HH(single co-polarization)
2. VV(single co-polarization)
3. VV (single co-polarization) + VH (dual-band cross-polarization)
4. HH (single co-polarization)+ HV (dual-band cross-polarization)

The brightness in each pixel is typically represented in σ° (sigma-naught), which is calculated from backscatter amplitude and expressed in decibel (dB).In the preprocessing operation, GEE utilizes the same preprocessing steps implemented by the Sentinel-1 Toolbox to derive the backscatter coefficient(σ°) in decibels (dB) in each pixel, which includes the following preprocessing steps(Vollrath et al., 2020):

- Apply orbit file
- Remove GRD border noise
- Remove thermal noise
- Radiometric calibration
- Range-Doppler Terrain correction (orthorectification)

The backscatter coefficient indicates whether the illuminated targets on the Earth's surface by the microwave energy scatter the incident radiation towards the SAR sensor (dB>0) or away from the SAR sensor (dB<0) (Sentinel-1 Algorithms | Google Earth Engine).

It is worth noting that GEE does not perform a thorough preprocessing operation. That is because it may vary from one application to another and, most importantly, enable the user to adapt and optimize the preprocessing steps according to its application's purpose. For inland water applications, additional preprocessing steps such as speckle filtering should be performed by the user to efficiently prepare the SAR images for information extraction, as recommended by Committee on Earth Observation Society (CEOS) Analysis-Ready-Data for Land (CARD4L)(Mullissa et al., 2021).

4.2 Speckle Filtering

A speckle is a form of noise (grainy salt-and-pepper texture) that appears in all SAR images and does not convey useful information when displayed in detail. When the radar signal is scattered by small features (i.e., small relative to wavelength), due to the signal coherence, it tends to either constructively interfere, creating bright returns, or destructively interfere, creating dark returns. Speckle significantly increases the complexity of the image interpretation (visually and digitally) since it reduces the image's quality; therefore, it is recommended to filter it prior to interpretation and analysis.

There are two primary methods for speckle reduction: multi-look process and spatial filtering. The former is performed during the data acquisition by dividing the radar beam into narrower sub-beams, where each will provide an independent look at the targets. Speckle appears in each of these looks; thus, averaging them will reduce the effect of speckle in the final output image. The spatial filtering approach is performed on the Level-1 output image using image geometric processing techniques(e.g., the spatial convolution operation). These operations calculate a new brightness value for each pixel in the image by processing the brightness values of all the local neighbors by running a template or window (e.g., 3 x 3 or 5x5) over the image, pixel by pixel. The new pixel value mainly depends upon the mathematical calculation (e.g., average, median, or

mode) performed on the pixels under the moving window(Richards, 2022). The median operator is well suited to reduce the speckle and avoid edge deterioration(Figure 8).

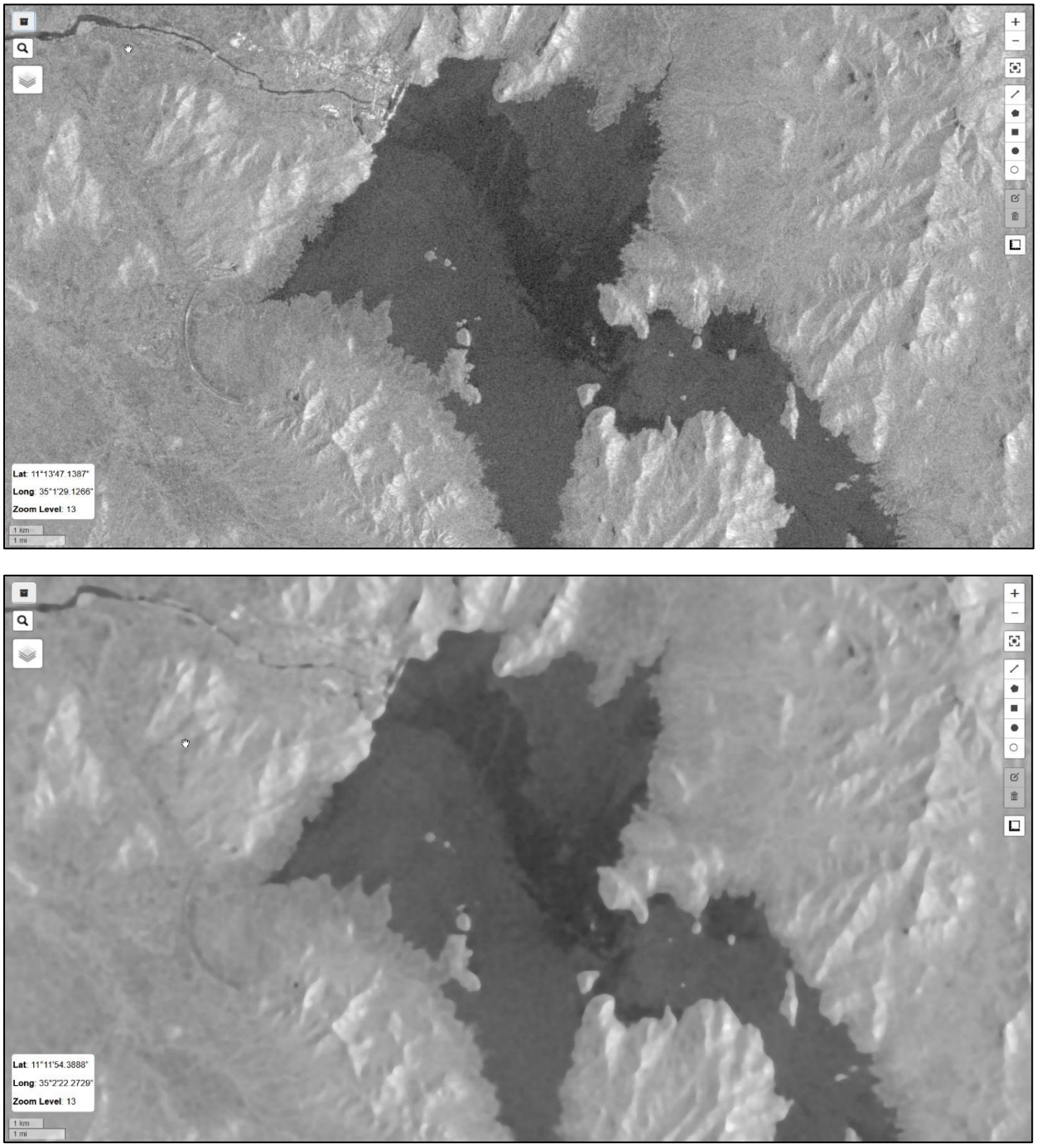

Figure 8. Speckle filtering using the median operator. Before(top), after(bottom). Sentinel-1 SAR images (VV) of the GERD reservoir (Acquired on 30 April 2022).

According to this operator, the new brightness value of the central pixel at the center of the moving window is the median value of all pixels under this window.

It is noteworthy that performing speckle filtering always comes at the expense of high spatial resolution. Those approaches essentially smooth the image, subjecting it to potentially eliminating its genuine high-frequency information. Therefore, the amount of speckle reduction performed should be balanced with the degree of details required for a particular application.

Generally, both speckle reduction approaches—multi-look process and median operator— belong either to non-adaptive or adaptive filters. The former is uniformly applied to the entire image and requires less computation, while the latter can preserve the natural edges by being adjusted to match the terrain's local properties(Introduction to Remote Sensing, 2011). Other adaptive filters include the Lee filter, Refined Lee filter, and the improved Lee sigma filter.

The Lee filter is one of the standard filters that have performed well in reducing speckles in SAR images, using the minimum mean square error (MMSE). Still, it may over smoothen the image texture, resulting in difficulties when boundaries and edge preservation is required. Therefore, Yommy et al. (2015) proposed refinement to the traditional Lee filter, namely the Refined Lee filter (Figure 9), employing the development in the K-Nearest Neighbor algorithm. Instead of using all neighbor pixels of the central pixel under the moving window, one can select some neighbor pixels less than the maximum. The suggested method achieved the best result when a moving window size of 3 x3 was employed, and only 6 out of 9 of the neighbor pixels were used.

Besides the median operator, the Refined lee filter is used in this work, and its code was adopted (Lemoine, 2018).

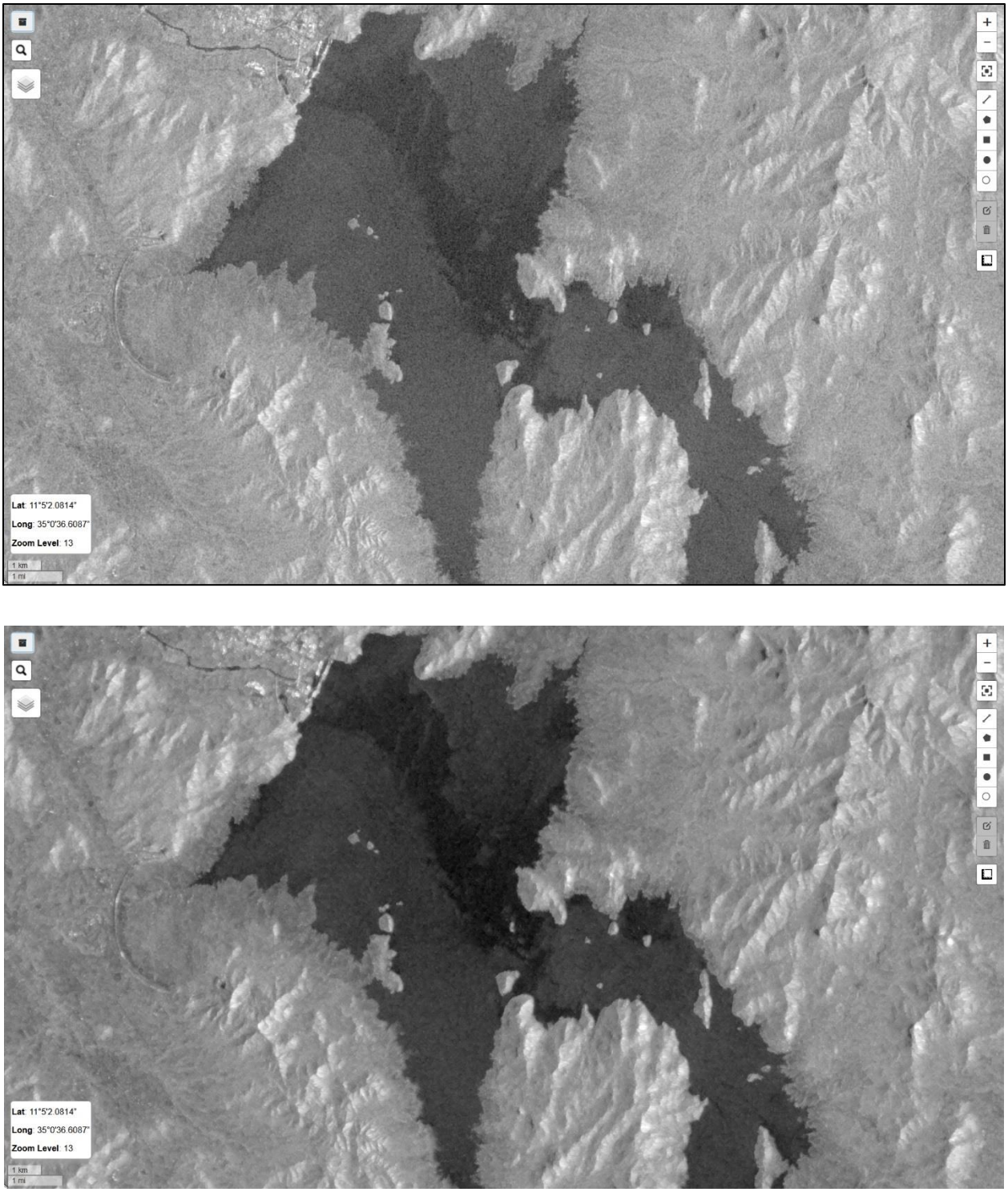

Figure 9. Speckle filtering using the Refined Lee filter. Before(top), after(bottom).

Sentinel-1 SAR images (VV) of the GERD reservoir (Acquired on 30 April 2022).

The image is displayed by the Iteru map interface in Jupyter Notebook.

5. Water Body Detection from Sentinel-1 SAR

5.1 Forward Scattering

The backscatter mechanism plays a critical role in accurately interpreting the SAR image content. Surface properties and roughness significantly determine whether the transmitted signal will scatter back towards the radar or away from it. In the case of a calm water surface, which is considered a smooth surface (relative to the signal wavelength), a forward scattering (specular reflection)(Figure 10) occurs where the transmitted signals illuminate the surface targets and mostly scatter away from the SAR antenna. Since only a little energy is reflected (low backscatter values), these targets appear as dark-toned areas on the image.

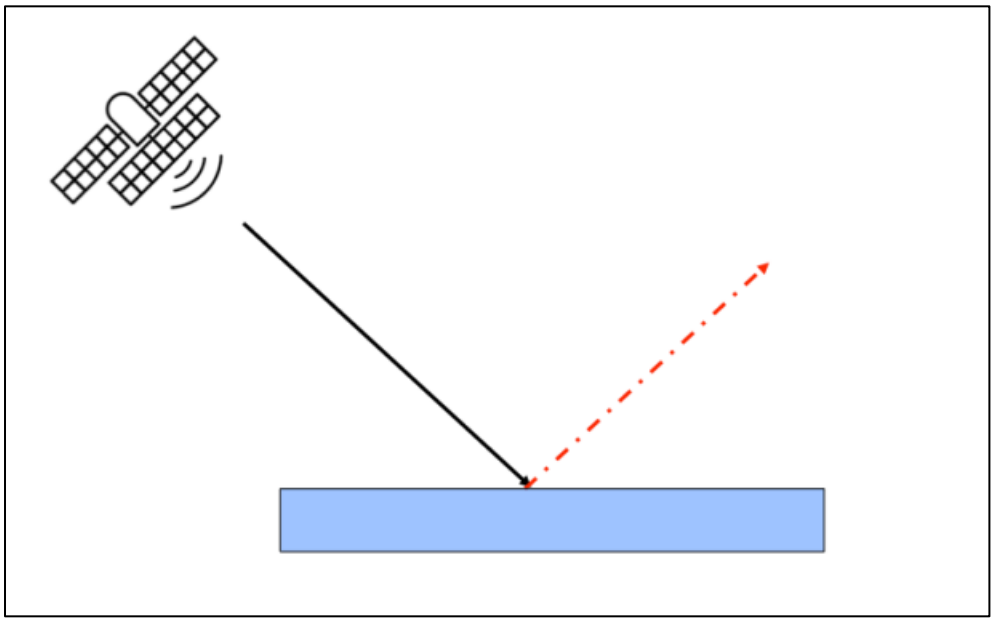

Figure 10. Forward scattering on a smooth surface (A Layman's Interpretation Guide to L-Band and C-Band Synthetic Aperture Radar Data, 2018)

Due to the forward scattering, the water body tends to have low backscatter values, appearing as a homogeneous dark area. In contrast, the non-water body tends to have higher backscatter values. Therefore, water bodies can be easily detected using the backscatter threshold that separates both classes.

5.2 Thresholding Technique

Various detection algorithms for SAR-based water bodies have been adopted, including thresholding, object-based image analysis, supervised and unsupervised classification techniques, and hybrid approaches(Bioresita et al., 2018). Among these approaches, the thresholding technique has been the most employed to distinguish water bodies from land in SAR imagery. Compared to other approaches, this technique has a fast computational speed; its results are reliable and satisfactory(Hahmann et al., 2008). All backscatter values lower than a given threshold are assigned to the water class, and others are assigned to the non-water class.

The threshold can be determined manually based on the SAR image histogram. However, in the case of processing multi-temporal images, custom thresholds need to be obtained for each SAR image individually. Since other factors such as wind-induced waves and incidence angle can vary the backscatter values from one image to another, requiring intensive work in case of a huge amount of data.

5.3 Otsu Thresholding

An automatic thresholding determination procedure can be performed using the Otsu thresholding, eliminating the need for user interaction. Otsu thresholding is a histogram-based thresholding approach, which is commonly used for image segmentation by maximizing the inter-class variance between two classes, foreground and background class. The water is the foreground class in this work, and the non-water (land) is the background class. This technique assumes the histogram of the pixels values has a bimodality distribution(Markert et al., 2020). It can efficiently determine an optimal threshold if the image has only two distinct classes. It is worth mentioning that this approach performs well if the foreground (water body) area constitutes more than 30% of the total image area; on the contrary, the performance efficiency decreases if it is less than 10%(Zhibin et al., 2019). Fortunately, this condition is satisfied in the study area of this work.

Figure 11 illustrates the bimodal distribution of the Sentinel-1 SAR image of the GRED reservoir after applying the Refined Lee filter, acquired on 30 April 2022. The histogram statistics were calculated using the Iteru package in Jupyter Notebook, showing that the backscatter values (dB)

range from -30.17 to 16.09. The reservoir surface water(Figure 12) was mapped after calculating the optimal threshold (-16.99 dB) using Otsu's method. Finally, the surface water generated map is a binary "water"/"non-water" image. Every pixel value less than this threshold was assigned to the water class and all other pixels were assigned to non-water and masked out.

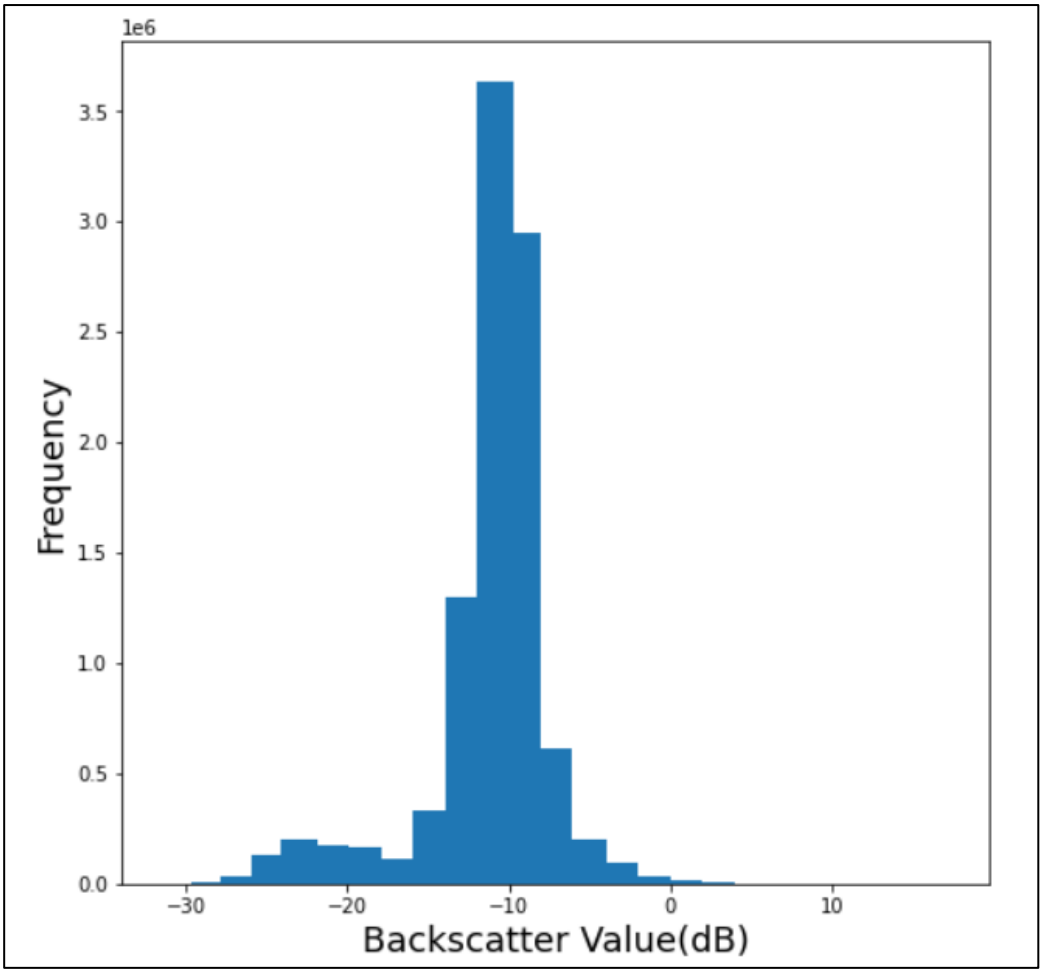

Figure 11. The bimodal distribution of Sentinel-1 SAR image of The GERD reservoir (Acquired on 30 April 2022).

It is important to note that some misclassification may occur, resulting in the salt-and-pepper effect, due to the presence of objects that are non-water but have low backscatter values similar to calm surface water, e.g., buildings, streets, and shadows in mountainous terrain. Thereby, a post-processing classification becomes necessary by applying morphological operations.

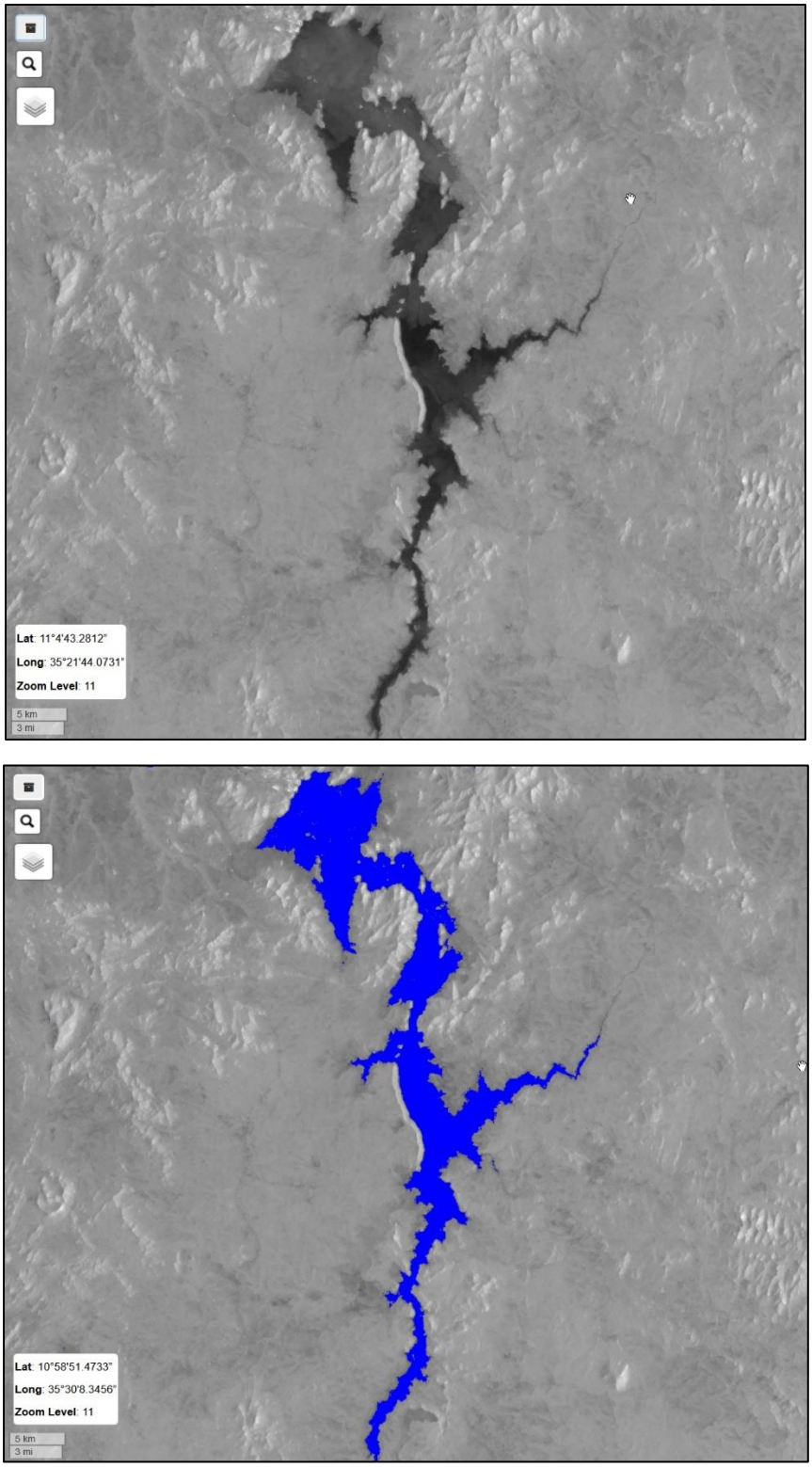

Figure 12. The final generated surface water map of the GERD reservoir using Otsu's threshold. The blue color represents the water body mapped using Otsu's threshold in the bottom image.

5.4 The suitability of VV and VH polarization

Inland waterbody can be detected using both VV and VH polarization from SAR scenes. Thus far, the studies comparing both polarizations' suitability for waterbody mapping are scarce. (Twele et al., 2016) evaluated the thematic accuracy of automatic surface water mapping and found that the C-band VV polarization slightly performs better than the C-band VH under calm wind conditions. However, the C-band VV backscatter can vary considerably during an intense storm event(Figure 13) since it is highly sensitive to the water surface roughness. In contrast, the C-band VH backscatter remains extremely slow in most cases(*A Layman's Interpretation Guide to L-Band and C-Band Synthetic Aperture Radar Data*, 2018).

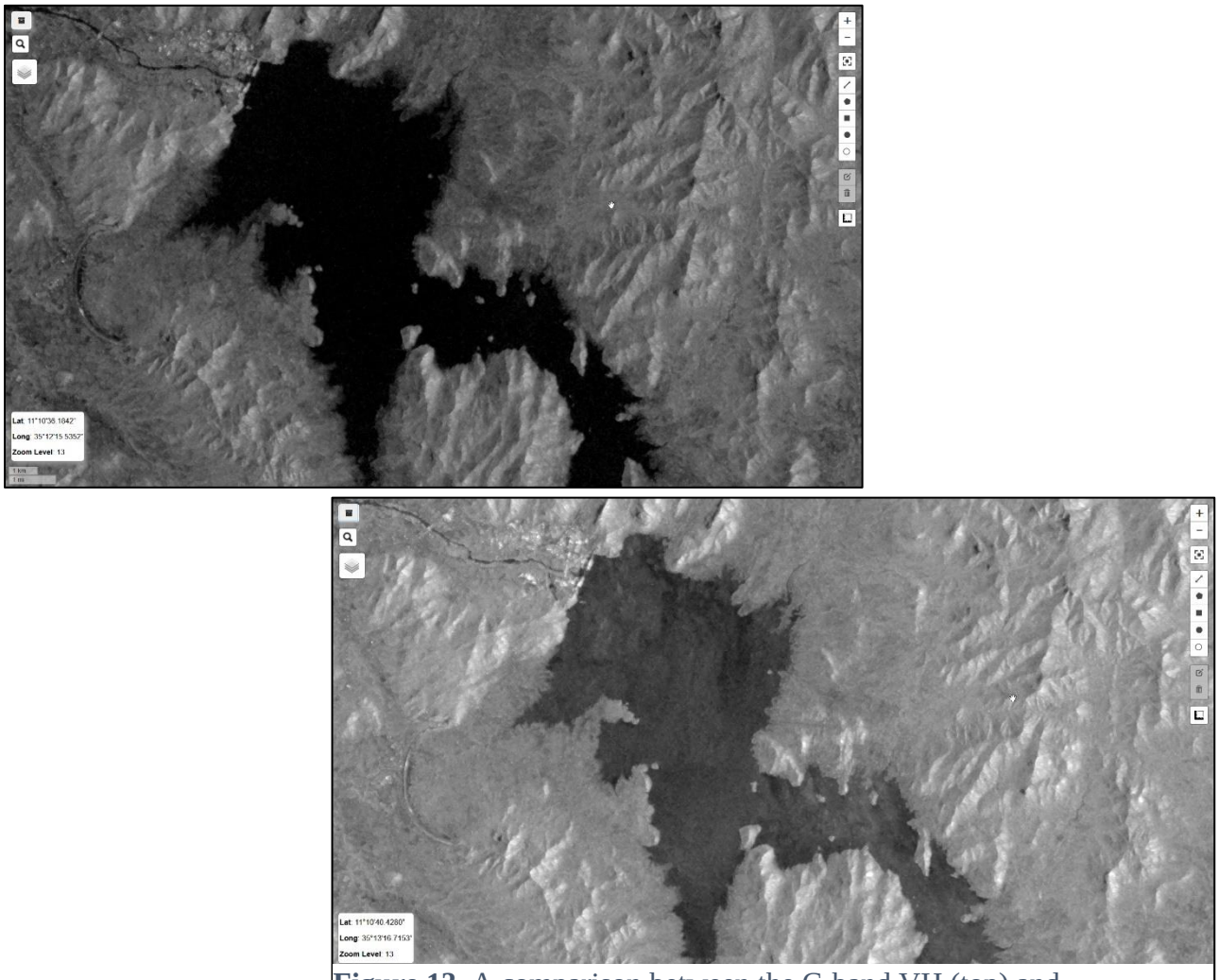

Figure 13. A comparison between the C-band VH (top) and VV(bottom) polarization sensitivity during a strong wind event. (Acquired on 29 January 2021)

6. Methodology (IteruApp Workflow)

IteruApp is an interactive, user-friendly web application designed to continuously monitor the GERD reservoir's surface water extent and water body volume using the GEE platform and Sentinel-1 SAR GRD imagery. Its primary purpose is to serve as a reliable source of information about the GERD reservoir water body for the public. It is built upon Iteru, a Python package that contains a collection of functions built upon GEE Python API and is mainly designed for this study area—the GERD reservoir—to perform the continuous monitoring.

The application independently performs two main tasks: creating a timelapse of the reservoir and calculating its waterbody statistics based on the timespan and other input parameters submitted by the user. Figure 13 demonstrates the workflow of the IteruApp processing chain. All the computations run on the fly in an automatic processing chain, starting with performing automatic data ingestion from the GEE data catalog, sending the required image analysis and computations to the GEE servers, and finally displaying the results, given valid input parameters from the user.

6.1 The Input Parameters

The input parameters define the criteria to perform the automatic dataset ingestion from the GEE data catalog and how to visualize the final results. It is composed of two main categories: data ingestion and timelapse.

The data ingestion parameters, defined by the user, include:

- The time frame: it includes the start date, which should not be before 1 July 2020, and the end date, which should not be after the date of usage day.
- The temporal frequency: the user can set it as native temporal resolution (12 days), monthly, or quarterly. The images of each month (monthly) or three months(quarterly) are reduced to a single output image, where each pixel in that image contains the median value of all the corresponding pixels' values. To demonstrate, typically, seven images are captured by the Sentinel-1 mission for the study area every three months. In the case of reducing these images using the median reducer, each pixel in the output image is composed of the median value of the seven corresponding pixels in all matching bands.

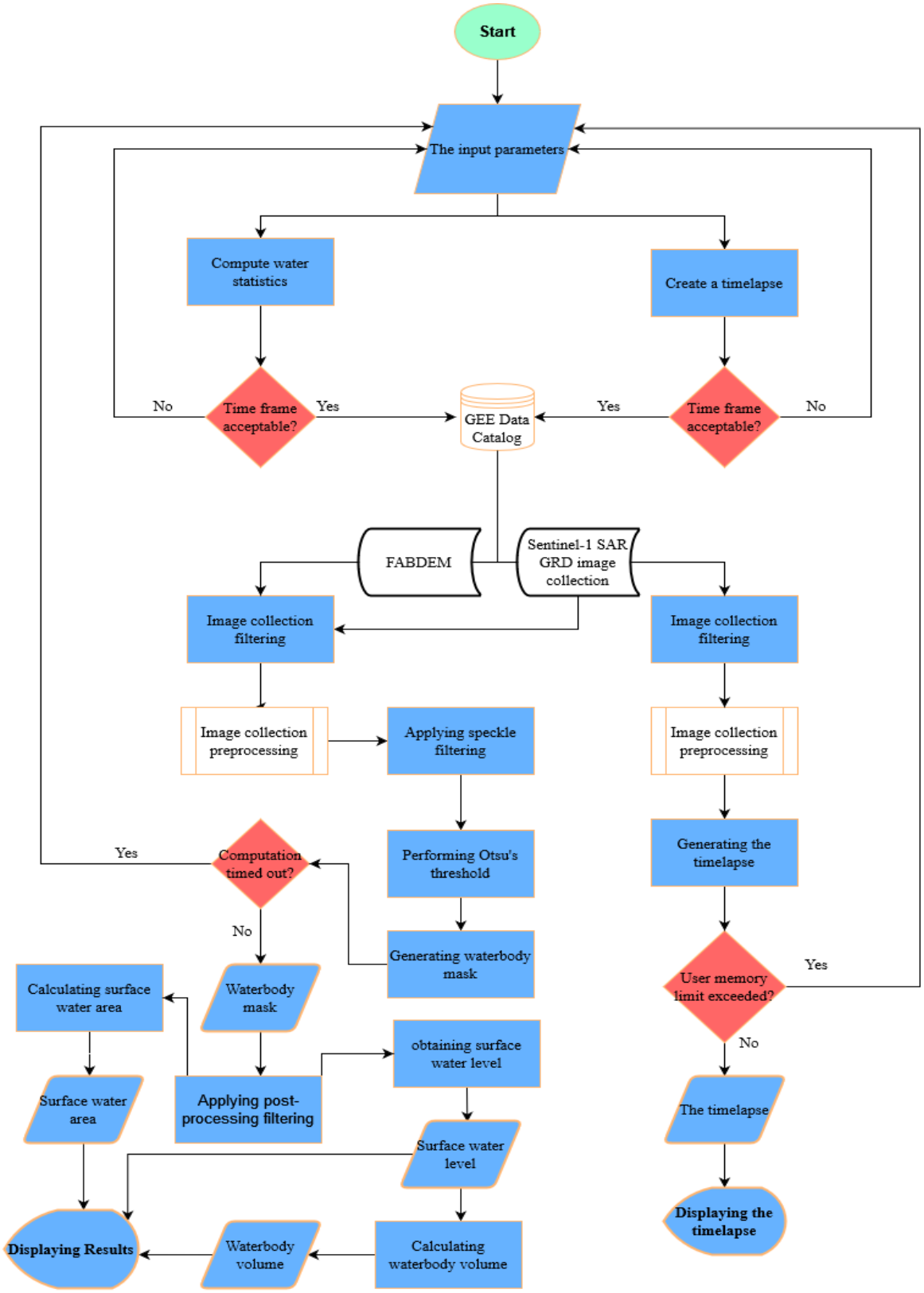

Figure 14. The workflow of the IteruApp processing chain.

The timelapse parameters include:

- The visualization methods(Figure 14): the visual representation can be produced with:
  - Single-band: VV, VH, or water mask
  - RGB representation (red: VV band, green: VH band, blue: VV/VH).
  - Mosaic of RGB and water mask
- Frame per second: the timelapse (animation) speed
- The timelapse labels: font size and color

6.2 Image Collection Filtering and Preprocessing

Once the user specifies an acceptable time frame, the sentinel-1 SAR GRD image collection is filtered based on this parameter and other predefined parameters pertaining to the geographical location of the study area and the image collection metadata. The metadata-based filtering aims to create a homogeneous subset of Sentinel-1 SAR imagery. That is because this image collection is acquired using various acquisition modes, polarization combinations, and spatial resolution during ascending and descending orbits. These metadata parameters include the following properties:

1. Polarization: The availability of a certain polarization combination depends on the geographical location. As a general principle, the HH or HH-VH combination is available for the polar and sea-ice zones, while the VV or VV-VH is available for all other observation zones. Based on that, SAR images available for the GERD reservoir contain only three bands: VV, VH, and incidence angle. Only VV and VH bands are in the processing chain.
2. The acquisition modes: As mentioned previously in Chapter 3, the Sentinel-1 mission operates in four acquisition modes. The interferometric wide swath (IW) is the primary mode for observation over land and coastal areas.
3. The spatial resolution: The Sentinel-1 SAR GRD images have three spatial resolutions: full, high, and medium. The utilized one in this work is the high resolution, which is 20×22 m and is resampled to pixel spacing of 10×10m.

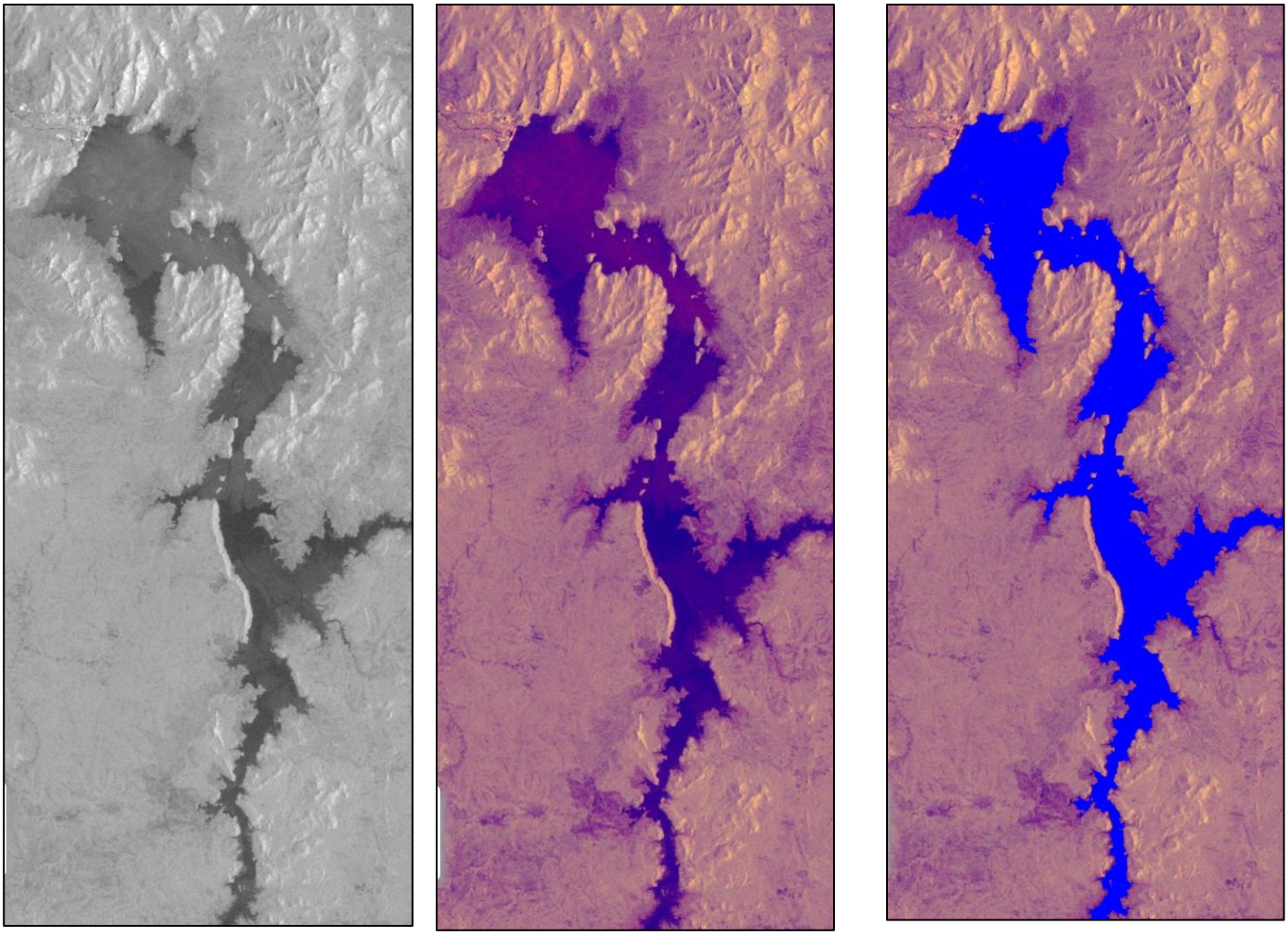

(a) (b) (c)

Figure 15. The timelapse visual representation options: (a) Single-band VV (b) RGB(red: VV, green: VH, blue: VV/VH) (c) RGB and water mask

- The orbit pass: Sentinel-1 is a polar-orbiting platform, and its scenes are acquired in two different obit passes: ascending (from the South Pole to the north pole) and descending(from the North Pole to the South Pole). The images available for the study area are in the descending orbit pass.
- The relative orbit number: This property of scenes metadata contains the orbit sequence number in the 12-day revisit cycle(175 orbits in 12 days). Therefore, images with the same relative orbit number are precisely 12 days apart with the same viewing configuration. The study area scenes are observed by the relative orbit number of 50.

In summary, for both tasks: creating a timelapse and computing water statistics, IteruApp filters the Sentinel-1 SAR image collection on the fly during the data ingestion step according to user-defined parameters, such as time frame and temporal frequency, and based on predefined parameters, including the geographic location of the study area, polarization combinations, acquisition modes, spatial resolution, and orbit properties. Simultaneously, GEE automatically performs all the preprocessing steps mentioned in Chapter 4 to derive the backscatter coefficient for each pixel.

6.3 Generating the Timelapse

Once implementing the filtering and preprocessing of the image collection, IteruApp generates a time series animation from all the selected images, where each image represents a frame, adding the image acquisition date and the Copywrite information to each frame. The visualization method parameter determines which band to select for the visual representation. The frame-per-second parameter controls the animation speed, ranging from displaying one frame a second to five frames a second. If all the timelapse parameters are acceptable, the animation is generated and displayed in a few seconds.

6.4 User Memory Limit Exceedance

Along with the number of images requested, the animation dimension parameter can cause an error (memory limit exceeded). This parameter determines the maximum number of dimensions (in pixels) to render each image. In any attempt to create a timelapse, if the number of pixels exceeds one hundred million pixels, this will raise an error of memory limit exceedance. Consequently, the processing chain stops immediately, and a warning message appears asking the user to reduce the time frame or the animation dimensions of rendering.

6.5 Compute Water Statistics

The processing chain of the computing water statistics task starts from determining the time frame—the start date and end date—and the temporal frequency from the input parameters. Consequently, the Sentinel-1 SAR image collection is automatically filtered and preprocessed based on the user-defined and predefined parameters. An additional preprocessing step is

implemented; speckle filtering is performed for each image to reduce the salt-and-pepper noise. Iteru package provides two functions to reduce the SAR images speckle: the median operator and the Refined Lee filter. The median filter is a simple way to reduce the image noise in a shorter computation time. Using the GEE platform, it approximately takes less than five minutes to apply the median filter on 57 of the SAR scenes of the study area. However, it has less effective performance since it is uniformly applied to the entire image, regardless of its terrain properties, degrading the radiometric and spatial resolution, which potentially eliminates valuable information from the scene. On the other hand, the Refined Lee filter is a more advanced technique to despeckle the noise while preserving the image's fine details. Compared with the median operator, the Refined Lee filter requires a longer computational time, raising a computational time-out error in case of applying to multiple images, exceeding the computations times more than five minutes.

To achieve an acceptable balance between the effectiveness and time consuming, the Refined Lee filter is employed to despeckle the noise of SAR images individually. Based on the time frame specified by the user, IteruApp shows the dates of SAR images available within that period. Accordingly, the user selects the image to be processed to calculate its water statistics.

After despeckling the noise, the waterbody can be extracted from each Sentinel-1 SAR scene using the automatic Otsu's or a local threshold, which typically ranges from -21 to -25 (dB) for C-band VH polarization. After that, a post-processing operation filters out all the misclassified pixels and retains only the reservoir water mask. Accordingly, the extracted water mask is incorporated with the DEM of FABDEM to determine the surface water level and ground elevation for each pixel.

After that, the waterbody volume is calculated by a simple pixel-based volume estimation model. Each pixel volume is estimated based on its area (30 x 30 m) and the per-pixel change in elevation (the difference between the pixel ground elevation and the surface water level). Then, all pixel volumes are summed up to produce each scene's total water body volume. The pixel-based model volume calculation can be implemented with high-resolution grids, but an optimal grid size must be considered. Although there is no certain defined threshold of the acceptable margin error, keeping the margin below about 1% for a high-resolution grid is recommended. For that purpose, the pixel area should not exceed 0.0008% of the total area of the study area(Slavinić & Cvetković, 2016).

7. Experimental Results and Discussion

7.1 The Optimal Threshold and Area Statistics

The earlier methodology was applied to the GERD reservoir Sentinel-1 SAR scenes between 1 July 2020(the first filling phase) and 30 April 2022, where 54 images were acquired for this study area. The VV and VH polarization bands were employed individually in the processing chain to compare their effectiveness in surface water mapping. Therefore, two water masks were extracted from each image; subsequently, two waterbody statistics were computed.

Figure 16 illustrates the two Otsu thresholds obtained for each scene. For the VV polarization band, the threshold that distinguishes the water from the non-water elements ranges from -16.87 to -14.37, while it ranges from -23.12 to -20.87 for the VH polarization band. Each threshold was applied to its corresponding band to extract the water mask; then, a post-processing operation was performed to remove all the misclassified water elements before calculating the area of each water mask.

To summarize, two water masks can be extracted from each image using the VV and VH bands. The area calculated from each mask varies because both polarizations interact differently with the targets on the Earth's surface. For instance, the latest image available was acquired on 30 April 2022. For that image, the optimal threshold to extract waterbody from its VV and VH bands is -15.87 and -22.62, respectively. Based on that, the calculated area of the water mask generated from the VV and VH band is 267.04 and 311.95 km^2, respectively. Figure 17 demonstrates significant differences between the calculated water mask area of the same image, as the latest image indicated.

The water mask area is the most critical variable in the processing chain. It accurately indicates whether the water storage increases or decreases and equally importantly, based on it, the surface water level and the waterbody volume are calculated. Therefore, an accuracy assessment was performed to evaluate the effectiveness of the VV and VH bands in surface water mapping and to infer which band has an effective and functional performance to be utilized to calculate the other variables.

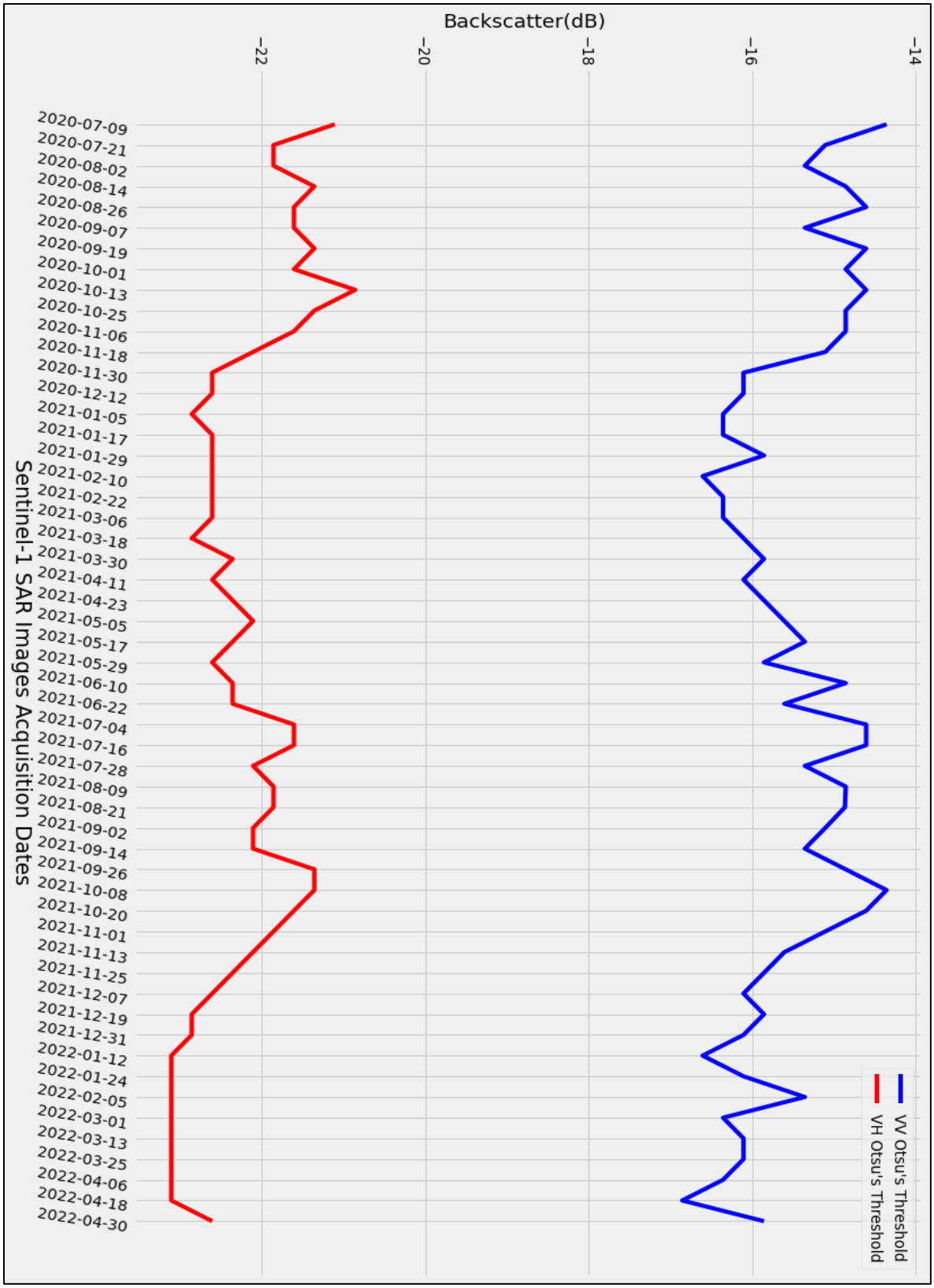

Figure 16.*The generated Otsu's threshold for the 54 Sentinel-1 SAR scenes for both VV and VH polarizations.*

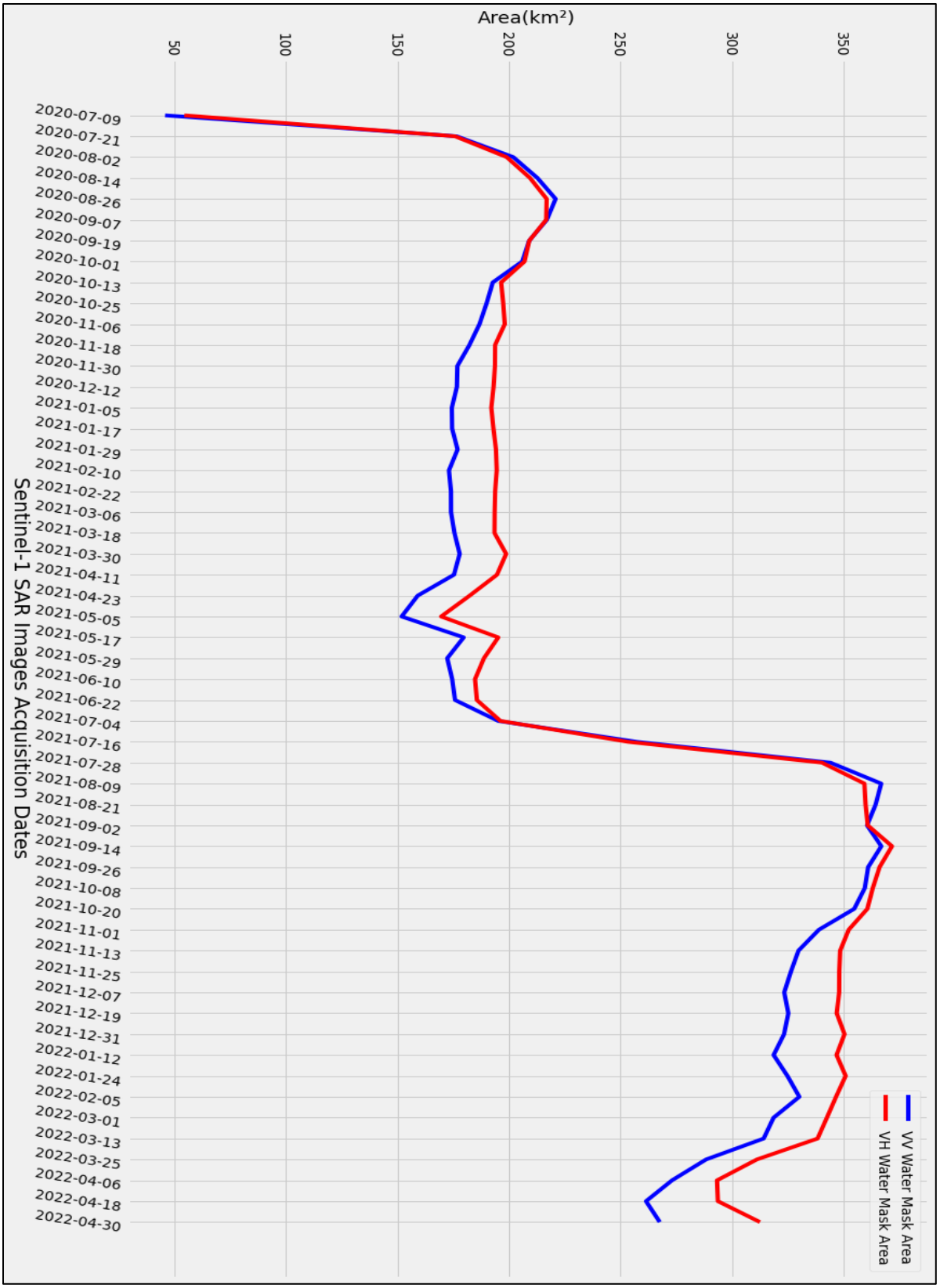

Figure 17. The area (km2)of each water surface extent for both the VV and VH polarization

7.2 Accuracy Assessment

The effectiveness of utilizing VV and VH polarization bands in surface water mapping was evaluated by comparing the extracted water mask from each to the Sentinel-2-based validation dataset by visual interpretation. To guarantee high accuracy for the generated reference points, the Sentinel-2 scenes were selected specifically to meet the following criteria:

1. The Sentinel-2 scenes should be almost cloudless and acquired on the same day as the corresponding Sentinel-1 scene or one day apart at most.
2. The Sentinel-1 scenes, which show significant differences between the calculated area from VV and VH bands, have more priority to be evaluated.

In table 2, the Sentinel-2 scenes which met the criteria mentioned above are listed. The table shows the acquisition date of the corresponding scenes and the cloud percentage in each Sentinel-2 scene.

One thousand reference points were generated using a simple random approach in each image of the GERD reservoir distributed proportionally over the water and non-water pixels. Then, these points were classified into water/non-water classes by visually interpreting the Sentinel-2 images. The performance of the VV and VH bands in surface water mapping was evaluated using these classified reference points.

Table 2. The Sentinel-2 scenes metadata were used for the accuracy assessment.

Samples Number	Sentinel-2 Scene Acquisition Date	Cloud (%)	Sentinel-1 Scene Acquisition Date
1	26-10-2020	7.3	25-10-2020
2	30-11-2020	0	30-11-2020
3	29-01-2021	1.18	29-01-2021
4	05-03-2021	1.67	06-03-2021
5	25-11-2021	0	25-11-2021
6	30-12-2021	9.45	31-12-2021
7	28-02-2022	0	01-03-2022
8	29-04-2022	0.7	30-04-2022

Tables 3 to 10 summarize the thematic accuracy assessment of the surface water maps extracted from Sentinel-1 SAR imagery by comparison between the performance of VV and VH polarization bands.

Table 3. Overall, producer's, user's accuracies, and kappa coefficient for validation Sentinel-1 SAR scene acquired on 25-10-2020.

	VV Polarization	Referenced		
	Classes	Water	Non-water	Total
Classified	Water	247	8	255
	Non-Water	15	730	745
	Total	262	738	1000
	Overall Accuracy	**97.7%**		
Water	User's Accuracy	96.9%		
	Producer's Accuracy	94.3%		
Non-water	User's Accuracy	98.0%		
	Producer's Accuracy	98.9%		
	Kappa	**0.94**		

	VH Polarization			
	Classes	Water	Non-water	Total
	Water	241	12	253
	Non-Water	21	726	747
	Total	262	738	1000
	Overall Accuracy	**96.7%**		
Water	User's Accuracy	95.3%		
	Producer's Accuracy	92.0%		
Non-water	User's Accuracy	97.2%		
	Producer's Accuracy	98.4%		
	Kappa	**0.91**		

Table 4. Overall, producer's, user's accuracies, and kappa coefficient for validation Sentinel-1 SAR scene acquired on 30-11-2020.

	VV Polarization	Referenced		
	Classes	Water	Non-water	Total
Classified	Water	256	2	258
	Non-Water	13	729	742
	Total	269	731	1000
	Overall Accuracy	**98.5%**		
Water	User's Accuracy	99.2%		
	Producer's Accuracy	95.2%		
Non-water	User's Accuracy	98.2%		
	Producer's Accuracy	99.7%		
	Kappa	**0.96**		

	VH Polarization			
	Classes	Water	Non-water	Total
	Water	261	26	287
	Non-Water	8	705	713
	Total	269	731	1000
	Overall Accuracy	**96.6%**		
Water	User's Accuracy	90.9%		
	Producer's Accuracy	97.0%		
Non-water	User's Accuracy	98.9%		
	Producer's Accuracy	96.4%		
	Kappa	**0.92**		

Table 5. Overall, producer's, user's accuracies, and kappa coefficient for validation Sentinel-1 SAR scene acquired on 29-01-2021.

	VV Polarization	Referenced		
	Classes	Water	Non-water	Total
Classified	Water	254	4	258
	Non-Water	9	733	742
	Total	263	737	1000
	Overall Accuracy	**98.7%**		
Water	User's Accuracy	98.4%		
	Producer's Accuracy	96.6%		
Non-water	User's Accuracy	98.8%		
	Producer's Accuracy	99.5%		
	Kappa	**0.97**		

	VH Polarization			
	Classes	Water	Non-water	Total
	Water	259	19	278
	Non-Water	4	718	722
	Total	263	737	1000
	Overall Accuracy	**97.7%**		
Water	User's Accuracy	93.2%		
	Producer's Accuracy	98.5%		
Non-water	User's Accuracy	99.4%		
	Producer's Accuracy	97.4%		
	Kappa	**0.94**		

Table 6. Overall, producer's, user's accuracies, and kappa coefficient for validation Sentinel-1 SAR scene acquired on 06-03-2021.

	VV Polarization	Referenced		
	Classes	Water	Non-water	Total
Classified	Water	248	7	255
	Non-Water	14	731	745
	Total	262	738	1000
	Overall Accuracy	**97.9%**		
Water	User's Accuracy	97.3%		
	Producer's Accuracy	94.7%		
Non-water	User's Accuracy	98.1%		
	Producer's Accuracy	99.1%		
	Kappa	**0.95**		

	VH Polarization			
	Classes	Water	Non-water	Total
	Water	261	19	280
	Non-Water	1	719	720
	Total	262	738	1000
	Overall Accuracy	**98.0%**		
Water	User's Accuracy	93.2%		
	Producer's Accuracy	99.6%		
Non-water	User's Accuracy	99.9%		
	Producer's Accuracy	97.4%		
	Kappa	**0.95**		

Table 7. Overall, producer's, user's accuracies, and kappa coefficient for validation Sentinel-1 SAR scene acquired on 25-11-2021.

	VV Polarization	Referenced		
	Classes	Water	Non-water	Total
Classified	Water	421	15	436
	Non-Water	11	553	564
	Total	432	568	1000
	Overall Accuracy	**97.4%**		
Water	User's Accuracy	96.6%		
	Producer's Accuracy	97.5%		
Non-water	User's Accuracy	98.0%		
	Producer's Accuracy	97.4%		
	Kappa	**0.95**		

	VH Polarization			
	Classes	Water	Non-water	Total
	Water	417	28	445
	Non-Water	15	540	555
	Total	432	568	1000
	Overall Accuracy	**95.7%**		
Water	User's Accuracy	93.7%		
	Producer's Accuracy	96.5%		
Non-water	User's Accuracy	97.3%		
	Producer's Accuracy	95.1%		
	Kappa	**0.91**		

Table 8. Overall, producer's, user's accuracies, and kappa coefficient for validation Sentinel-1 SAR scene acquired on 30-12-202.

	VV Polarization	Referenced		
	Classes	Water	Non-water	Total
Classified	Water	339	2	341
	Non-Water	13	646	659
	Total	352	648	1000
	Overall Accuracy	**98.5%**		
Water	User's Accuracy	99.4%		
	Producer's Accuracy	96.3%		
Non-water	User's Accuracy	98.0%		
	Producer's Accuracy	99.7%		
	Kappa	**0.97**		

	VH Polarization			
	Classes	Water	Non-water	Total
	Water	346	10	356
	Non-Water	6	638	644
	Total	352	648	1000
	Overall Accuracy	**98.4%**		
Water	User's Accuracy	97.2%		
	Producer's Accuracy	98.3%		
Non-water	User's Accuracy	99.1%		
	Producer's Accuracy	98.5%		
	Kappa	**0.97**		

Table 9. Overall, producer's, user's accuracies, and kappa coefficient for validation Sentinel-1 SAR scene acquired on 01-03-2022.

	VV Polarization	Referenced		
	Classes	Water	Non-water	Total
Classified	Water	336	3	339
	Non-Water	9	652	661
	Total	345	655	1000
	Overall Accuracy	**98.8%**		
Water	User's Accuracy	99.1%		
	Producer's Accuracy	97.4%		
Non-water	User's Accuracy	98.6%		
	Producer's Accuracy	99.5%		
	Kappa	**0.97**		

	VH Polarization			
	Classes	Water	Non-water	Total
	Water	343	20	363
	Non-Water	2	635	637
	Total	345	655	1000
	Overall Accuracy	**97.8%**		
Water	User's Accuracy	94.5%		
	Producer's Accuracy	99.4%		
Non-water	User's Accuracy	99.7%		
	Producer's Accuracy	96.9%		
	Kappa	**0.95**		

Table 10. Overall, producer's, user's accuracies, and kappa coefficient for validation Sentinel-1 SAR scene acquired on 30-04-2022.

	VV Polarization			
	Classes	Water	Non-water	Total
	Water	359	10	369
	Non-Water	13	618	631
	Total	372	628	1000
	Overall Accuracy	**97.7%**		
Water	User's Accuracy	97.3%		
	Producer's Accuracy	96.5%		
Non-water	User's Accuracy	97.9%		
	Producer's Accuracy	98.4%		
	Kappa	**0.95**		

	VH Polarization			
	Classes	Water	Non-water	Total
	Water	368	55	423
	Non-Water	4	573	577
	Total	372	628	1000
	Overall Accuracy	**94.1%**		
Water	User's Accuracy	87.0%		
	Producer's Accuracy	98.9%		
Non-water	User's Accuracy	99.3%		
	Producer's Accuracy	91.2%		
	Kappa	**0.88**		

The accuracy assessment (Table 11) emphasized the conclusion (Twele et al., 2016) that the VV polarization slightly performs better than the VH polarization in surface water mapping from Sentinel-1 SAR imagery. The average kappa coefficient (k) of 0.96 for VV compared to 0.93 for VH polarization supports that conclusion. Furthermore, the average overall accuracy is in favor of the VV polarization where this band offers 98.2%, compared to 96.9% for the VH band. Regardless, the statistics of the individual classes obtained for the user's and producer's accuracies show considerable variability.

Statistically speaking, there is no significant difference between the compared results; however, there is a consideration regarding the VH polarization band. It always tends to misclassify many land pixels that are surrounding the waterbody as water pixels, increasing the area of the obtained surface water extent compared to the VV polarization band. This conclusion clarifies Figure 17, where the VH polarization band consistently generates a larger surface water area than the VV band. That behavior, in particular, makes the VV band outweigh the VH band to be utilized in the processing chain of IteruApp since the other statistics are calculated based on the water mask.

Table 11. The average of all accuracies assessments performed on the VV and VH bands of the selected eight scenes from Sentinel-1 SAR and Sentinel-2.

Accuracies	VV Polarization	VH Polarization
Kappa coefficient	0.96	0.93
Overall accuracy	98.2%	96.9%
Water user's accuracy	98%	93.1%
Water producer's accuracy	96%	97.5%
Non-water user's accuracy	98.2%	98.8%
Non-water producer's accuracy	99%	96.4%

7.3 Surface Water Level and waterbody Volume Statistics

Figures 18 and 19 compare VV and VH bands to obtain the reservoir surface water level and waterbody volume, respectively. The VV band provides more consistent and logical results, corresponding to the same reservoir waterbody volume obtained by other studies(Abou Samra & Ali, 2021; Kansara et al., 2021).

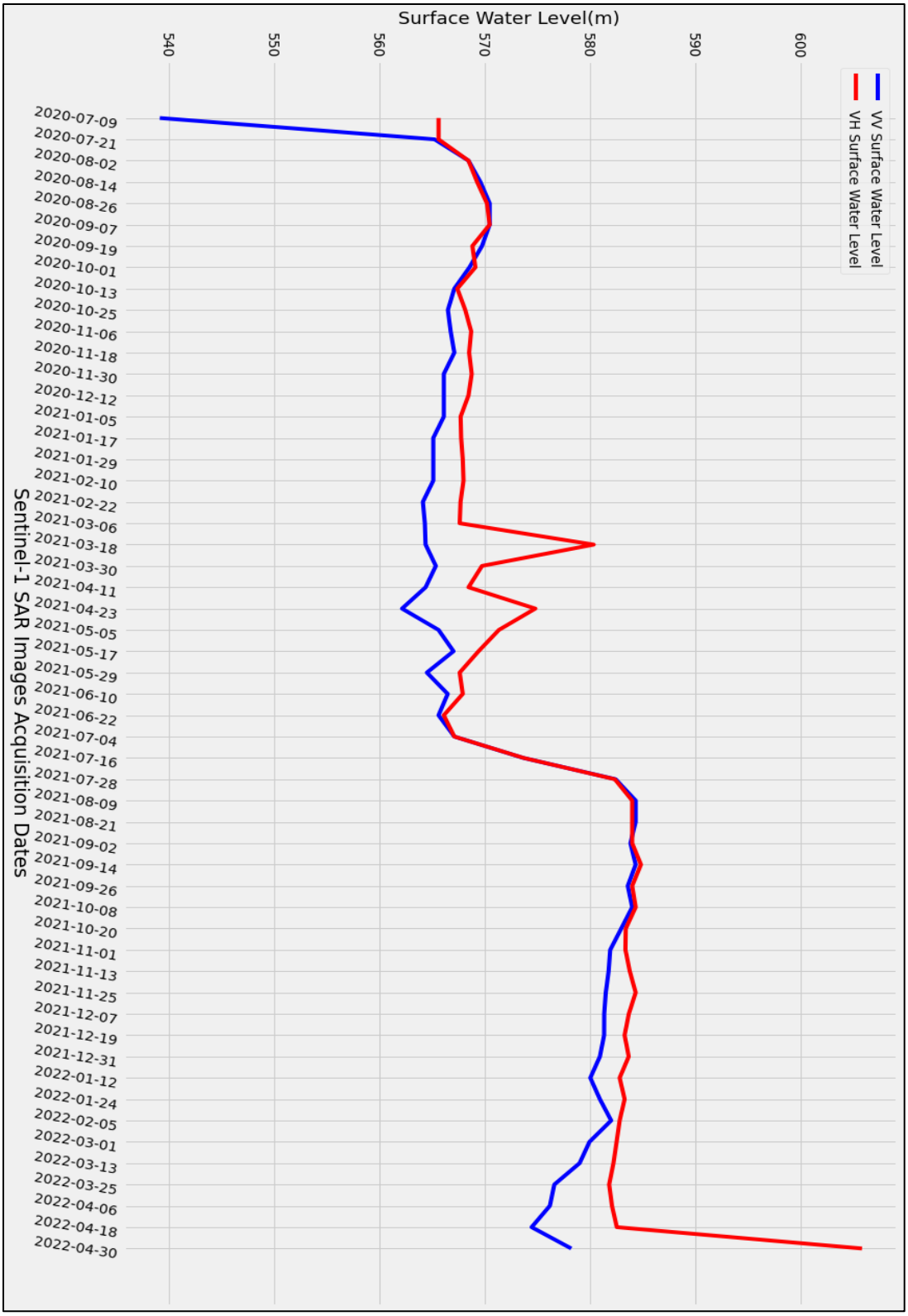

Figure 18. A comparison between the surface water level obtained from the VV and VH polarization bands.

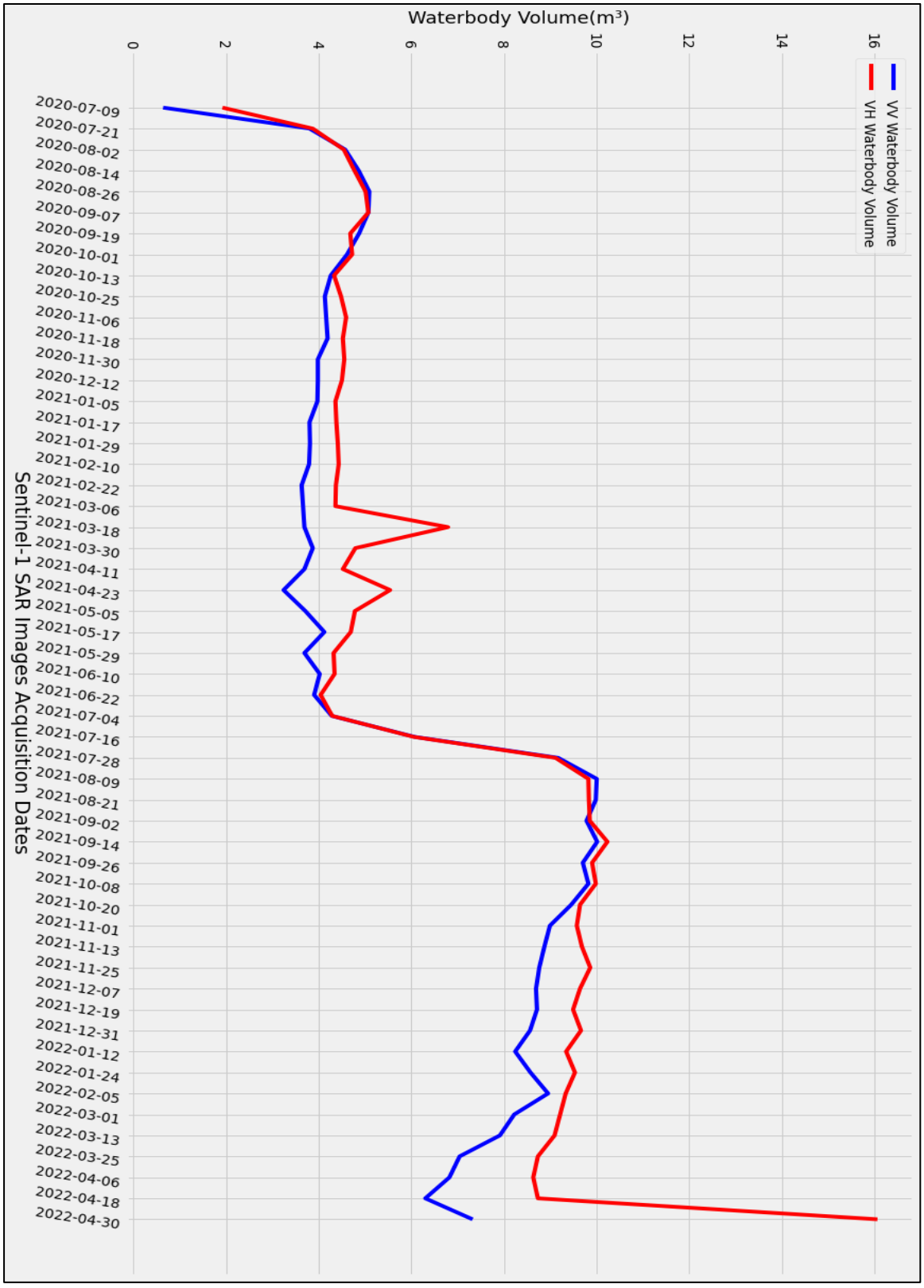

Figure 19. *A comparison between the waterbody volume obtained from the VV and VH polarization bands.*

Interestingly, the volume statistics obtained from the VV polarization band confirm the published news by the Ethiopian government about the first filling of the GERD reservoir, which was completed in July 2020. Figure 19 supports Ethiopia's claim that it managed to store approximately five billion m. Still, the graph contradicts the Ethiopian claim about the second filling completed in July 2021. Roughly ten billion m^3 were stored after the second filling, in opposition to 13.5 billion m^3 as announced by the Ethiopian government.

On the other hand, Figure 18 confirms the conclusion derived from the accuracy assessment of the VH polarization band. Its tendency to misclassify many land pixels surrounding the waterbody as water pixels caused an inconsistently increase in the obtained surface water level and subsequently the calculated volume of the reservoir waterbody.

8. Conclusion

In this work, we developed a user-friendly interactive web-based application (IteruApp) to continuously monitor the waterbody volume variation of the GERD reservoir in Ethiopia. The application is built upon Iteru, a Python package, which in turn is built upon the GEE Python API and leverages its powerful computational capabilities and continuously updated dataset catalog. The package can be installed and used in any development environment (e.g., Jupyter Notebook, Google Colab). The user-friendly application is hosted by Streamlit, an open-source framework for data science and machine learning applications.

This work employs two primary datasets from the GEE catalog: Sentinel-1 SAR C-band GRD image collection to map the reservoir surface water and FABDEM to calculate the surface water level and the waterbody volume.

The work evaluated the performance of the VV and VH polarization band in surface water mapping of the inland waterbody. The thematic accuracy assessment results suggest that VV polarization slightly outperforms the VH polarization with kappa coefficients ranging from 0.96 to 0.93 and overall accuracies between 98.2% and 96.9%.

Although the complexity of radar-based imagery, these sensors systematically provide high resolution, day-and-night, and weather-independent images. These advantages make radar imaging outperform optical imaging, especially in time-series analysis in regions with persistent cloud cover. This outperforming performance is strengthened by GEE's vital role in removing the intensive burden of many preprocessing steps and speeding up the multi-temporal analysis on a mass scale.

Further work should involve different polarization combinations (i.e., HH polarization) to map the surface water extent using other classification techniques and a more accurate validation dataset (e.g., commercial satellite imagery or UAV-based high-resolution imagery) to evaluate the thematic accuracy. Additionally, large-scale topographic maps would make the waterbody volume results more accurate.

Bibliography

A Layman's Interpretation Guide to L-band and C-band Synthetic Aperture Radar data. (2018).

Abou Samra, R. M., & Ali, R. R. (2021). Detection of the filling phases of the Grand Ethiopian Renaissance dam using sentinel-1 SAR data. *Egyptian Journal of Remote Sensing and Space Science*, *24*(3), 991–997. https://doi.org/10.1016/j.ejrs.2021.11.006

Beijing, Institute of Electrical and Electronics Engineers. Beijing Section, & Institute of Electrical and Electronics Engineers. *IEEE International Conference on Signal, Information and Data Processing 2019 : 11-13 December 2019 Chongqing, China*.

Bioresita, F., Puissant, A., Stumpf, A., & Malet, J. P. (2018). A method for automatic and rapid mapping of water surfaces from Sentinel-1 imagery. *Remote Sensing*, *10*(2). https://doi.org/10.3390/rs10020217

Egypt | United Nations Population Fund. (n.d.). Retrieved April 9, 2022, from https://www.unfpa.org/data/world-population/EG

Elsayed, H., Djordjević, S., Savić, D. A., Tsoukalas, I., & Makropoulos, C. (2020). The Nile Water-Food-Energy Nexus under Uncertainty: Impacts of the Grand Ethiopian Renaissance Dam. *Journal of Water Resources Planning and Management*, *146*(11), 04020085. https://doi.org/10.1061/(asce)wr.1943-5452.0001285

Ethiopia rejects Arab League resolution on Renaissance Dam | Arab League News | Al Jazeera. (n.d.). Retrieved April 11, 2022, from https://www.aljazeera.com/news/2021/6/16/ethiopia-rejects-arab-league-resolution-on-renaissance-dam

Gorelick, N., Hancher, M., Dixon, M., Ilyushchenko, S., Thau, D., & Moore, R. (2017). Google Earth Engine: Planetary-scale geospatial analysis for everyone. *Remote Sensing of Environment*, *202*, 18–27. https://doi.org/10.1016/j.rse.2017.06.031

Hahmann, T., Martinis, S., Twele, A., Roth, A., & Buchroithner, M. (n.d.). *Extraction of water and flood areas from SAR data*.

Hawker, L., Uhe, P., Paulo, L., Sosa, J., Savage, J., Sampson, C., & Neal, J. (2022). A 30 m global map of elevation with forests and buildings removed. *Environmental Research Letters*, *17*(2). https://doi.org/10.1088/1748-9326/ac4d4f

Introduction to Remote Sensing. (n.d.).

Jiang, H., Wang, M., Hu, H., & Xu, J. (2021). Evaluating the performance of sentinel-1a and sentinel-2 in small waterbody mapping over urban and mountainous regions. *Water (Switzerland)*, *13*(7). https://doi.org/10.3390/w13070945

Kansara, P., Li, W., El-Askary, H., Lakshmi, V., Piechota, T., Struppa, D., & Sayed, M. A. (2021). An assessment of the filling process of the grand Ethiopian renaissance dam and its impact on the downstream countries. *Remote Sensing*, *13*(4), 1–17. https://doi.org/10.3390/rs13040711

The Refined Lee filter algorithm - Earth Engine Code Editor. (2022). Retrieved May 2, 2022, from https://code.earthengine.google.com/5d1ed0a0f0417f098fdfd2fa137c3d0c

Markert, K. N., Markert, A. M., Mayer, T., Nauman, C., Haag, A., Poortinga, A., Bhandari, B., Thwal, N. S., Kunlamai, T., Chishtie, F., Kwant, M., Phongsapan, K., Clinton, N., Towashiraporn, P., & Saah, D. (2020). Comparing Sentinel-1 surface water mapping algorithms and radiometric terrain correction processing in southeast Asia utilizing Google Earth Engine. *Remote Sensing*, *12*(15). https://doi.org/10.3390/RS12152469

Mullissa, A., Vollrath, A., Odongo-Braun, C., Slagter, B., Balling, J., Gou, Y., Gorelick, N., & Reiche, J. (2021). Sentinel-1 sar backscatter analysis ready data preparation in google earth engine. *Remote Sensing*, *13*(10). https://doi.org/10.3390/rs13101954

Radar Polarimetry. (2020). Retrieved April 21, 2022, from https://www.nrcan.gc.ca/maps-tools-and-publications/satellite-imagery-and-air-photos/tutorial-fundamentals-remote-sensing/microwave-remote-sensing/radar-polarimetry/9275

Richards, J. A. (2022). Remote Sensing Digital Image Analysis. In *Remote Sensing Digital Image Analysis*. Springer International Publishing. https://doi.org/10.1007/978-3-030-82327-6

Roussi, A. (2019). Gigantic Nile dam prompts clash between Egypt and Ethiopia. *Nature*, *574*(7777), 159–160. https://doi.org/10.1038/D41586-019-02987-6

Sentinel-1 Algorithms | Google Earth Engine | Google Developers. (n.d.). Retrieved April 29, 2022, from https://developers.google.com/earth-engine/guides/sentinel1?hl=en

Sentinel-1 SAR GRD: C-band Synthetic Aperture Radar Ground Range Detected, log scaling | Earth Engine Data Catalog | Google Developers. (2022). Retrieved April 29, 2022, from https://developers.google.com/earth-engine/datasets/catalog/COPERNICUS_S1_GRD#description

Slavinić, P., & Cvetković, M. (2016). Volume calculation of subsurface structures and traps in hydrocarbon exploration - A comparison between numerical integration and cell-based models. *Open Geosciences*, *8*(3), 14–21. https://doi.org/10.1515/geo-2016-0003

Swain, A. (2011). Challenges for water sharing in the Nile basin: changing geo-politics and changing climate. *Https://Doi.Org/10.1080/02626667.2011.577037*, *56*(4), 687–702. https://doi.org/10.1080/02626667.2011.577037

THE SAR HANDBOOK Comprehensive Methodologies for Forest Monitoring and Biomass Estimation. (2018). https://doi.org/10.25966/nr2c-s697

Twele, A., Cao, W., Plank, S., & Martinis, S. (2016). Sentinel-1-based flood mapping: a fully automated processing chain. *International Journal of Remote Sensing*, *37*(13), 2990–3004. https://doi.org/10.1080/01431161.2016.1192304

User Guides - Sentinel-1 SAR - Acquisition Modes - Sentinel Online - Sentinel Online. (n.d.). Retrieved April 25, 2022, from https://sentinels.copernicus.eu/web/sentinel/user-guides/sentinel-1-sar/acquisition-modes

User Guides - Sentinel-1 SAR - Product Types and Processing Levels - Sentinel Online - Sentinel Online. (n.d.). Retrieved April 26, 2022, from https://sentinels.copernicus.eu/web/sentinel/user-guides/sentinel-1-sar/product-types-processing-levels

Vollrath, A., Mullissa, A., & Reiche, J. (2020). Angular-based radiometric slope correction for Sentinel-1 on google earth engine. *Remote Sensing*, *12*(11). https://doi.org/10.3390/rs12111867

World Development Indicators | The World Bank. (2017). Retrieved April 9, 2022, from http://wdi.worldbank.org/table/3.5

Yommy, A. S., Liu, R., & Wu, A. S. (2015). SAR image despeckling using refined lee filter. *Proceedings - 2015 7th International Conference on Intelligent Human-Machine Systems and Cybernetics, IHMSC 2015*, *2*, 260–265. https://doi.org/10.1109/IHMSC.2015.236

Acknowledgment

I want to express my gratitude to my supervisor, prof. András Jung, for his continuous guidance throughout my research and encouraging feedback. Again, I want to express my gratitude to him for his teaching method and kind attitude and for introducing new research topics to me in geospatial data science during his courses.

Declaration

I, Muhammed Ahmed Sayed Abdelaal(E5H5W3), declare that the present master's thesis is my original intellectual product in full and that I have not submitted any part or the whole of this work to any other institution. Permissions related to the use of copyrighted sources in this work are attached.

I agree to the publication of the accepted master's thesis in pdf form on the website of the Department of Cartography and Geoinformatics.

Budapest, *15,05,2022*